PHYSICAL REVIEW D VOLUME 43, NUMBER 7 1 APRIL 1991

ARTICLES

Measurement of the W-boson mass in 1.8-TeV $\bar{p}p$ collisions

F. Abe,[h] D. Amidei,[d] G. Apollinari,[k] M. Atac,[d] P. Auchincloss,[n] A. R. Baden,[f]
A. Bamberger,[d,*] A. Barbaro-Galtieri,[i] V. E. Barnes,[l] F. Bedeschi,[k] S. Behrends,[b] S. Belforte,[k] G. Bellettini,[k]
J. Bellinger,[r] J. Bensinger,[b] A. Beretvas,[d] J. P. Berge,[d] S. Bertolucci,[e] S. Bhadra,[g] M. Binkley,[d]
R. Blair,[a] C. Blocker,[b] A. W. Booth,[d] G. Brandenburg,[f] D. Brown,[f] E. Buckley,[n] A. Byon,[l]
K. L. Byrum,[r] C. Campagnari,[c] M. Campbell,[c] R. Carey,[f] W. Carithers,[i] D. Carlsmith,[r] J. T. Carroll,[d]
R. Cashmore,[d,†] F. Cervelli,[k] K. Chadwick,[d] G. Chiarelli,[e] W. Chinowsky,[i] S. Cihangir,[d] A. G. Clark,[d]
D. Connor,[j] M. Contreras,[b] J. Cooper,[d] M. Cordelli,[e] D. Crane,[d] M. Curatolo,[e] C. Day,[d]
S. Dell'Agnello,[k] M. Dell'Orso,[k] L. Demortier,[b] P. F. Derwent,[c] T. Devlin,[n] D. DiBitonto,[o] R. B. Drucker,[i]
J. E. Elias,[d] R. Ely,[i] S. Errede,[g] B. Esposito,[e] B. Flaugher,[n] G. W. Foster,[d] M. Franklin,[f]
J. Freeman,[d] H. Frisch,[c] Y. Fukui,[h] Y. Funayama,[p] A. F. Garfinkel,[l] A. Gauthier,[g] S. Geer,[f]
P. Giannetti,[k] N. Giokaris,[m] P. Giromini,[e] L. Gladney,[j] M. Gold,[i] K. Goulianos,[m] H. Grassmann,[k]
C. Grosso-Pilcher,[c] C. Haber,[i] S. R. Hahn,[d] R. Handler,[r] K. Hara,[p] R. M. Harris,[i] J. Hauser,[c]
T. Hessing,[o] R. Hollebeek,[j] L. Holloway,[g] P. Hu,[n] B. Hubbard,[i] B. T. Huffman,[l] R. Hughes,[j]
P. Hurst,[g] J. Huth,[d] M. Incagli,[k] T. Ino,[p] H. Iso,[p] H. Jensen,[d] C. P. Jessop,[f]
R. P. Johnson,[d] U. Joshi,[d] R. W. Kadel,[d] T. Kamon,[o] S. Kanda,[p] D. A. Kardelis,[g] I. Karliner,[g]
E. Kearns,[f] R. Kephart,[d] P. Kesten,[b] R. M. Keup,[g] H. Keutelian,[g] S. Kim,[p] L. Kirsch,[b]
K. Kondo,[p] S. E. Kuhlmann,[a] E. Kuns,[n] A. T. Laasanen,[l] J. I. Lamoureux,[r] W. Li,[a] T. M. Liss,[f]
N. Lockyer,[j] C. B. Luchini,[g] P. Maas,[d] M. Mangano,[k] J. P. Marriner,[d] R. Markeloff,[r] L. A. Markosky,[r]
R. Mattingly,[b] P. McIntyre,[o] A. Menzione,[k] T. Meyer,[o] S. Mikamo,[h] M. Miller,[c] T. Mimashi,[p]
S. Miscetti,[e] M. Mishina,[b] S. Miyashita,[p] Y. Morita,[p] S. Moulding,[b] A. Mukherjee,[d] L. F. Nakae,[b]
I. Nakano,[p] C. Nelson,[d] C. Newman-Holmes,[d] J. S. T. Ng,[f] M. Ninomiya,[p] L. Nodulman,[a] S. Ogawa,[p]
R. Paoletti,[k] A. Para,[d] E. Pare,[f] J. Patrick,[d] T. J. Phillips,[f] R. Plunkett,[d] L. Pondrom,[r]
J. Proudfoot,[a] G. Punzi,[k] D. Quarrie,[d] K. Ragan,[j] G. Redlinger,[c] J. Rhoades,[r] M. Roach,[q]
F. Rimondi,[d,‡] L. Ristori,[k] T. Rohaly,[j] A. Roodman,[c] D. Saltzberg,[c] A. Sansoni,[e] R. D. Sard,[g]
A. Savoy-Navarro,[d] V. Scarpine,[g] P. Schlabach,[g] E. E. Schmidt,[d] M. H. Schub,[l] R. Schwitters,[f] A. Scribano,[k]
S. Segler,[d] Y. Seiya,[p] M. Sekiguchi,[p] P. Sestini,[k] M. Shapiro,[f] M. Sheaff,[r] M. Shochet,[c]
J. Siegrist,[i] P. Sinervo,[j] J. Skarha,[r] K. Sliwa,[q] D. A. Smith,[k] F. D. Snider,[c] R. St. Denis,[f]
A. Stefanini,[k] R. L. Swartz, Jr.,[g] M. Takano,[p] K. Takikawa,[p] S. Tarem,[b] D. Theriot,[d] M. Timko,[o]
P. Tipton,[i] S. Tkaczyk,[d] A. Tollestrup,[d] G. Tonelli,[k] J. Tonnison,[l] W. Trischuk,[f] Y. Tsay,[c]
F. Ukegawa,[p] D. Underwood,[a] R. Vidal,[d] R. G. Wagner,[a] R. L. Wagner,[d] J. Walsh,[j] T. Watts,[n]
R. Webb,[o] C. Wendt,[r] W. C. Wester III,[i] T. Westhusing,[k] S. N. White,[m] A. B. Wicklund,[a] H. H. Williams,[j]
B. L. Winer,[i] A. Yagil,[d] A. Yamashita,[p] K. Yasuoka,[p] G. P. Yeh,[d] J. Yoh,[d] M. Yokoyama,[p]
J. C. Yun,[d] and F. Zetti[k]

(CDF Collaboration)

[a]*Argonne National Laboratory, Argonne, Illinois 60439*
[b]*Brandeis University, Waltham, Massachusetts 02254*
[c]*University of Chicago, Chicago, Illinois 60637*
[d]*Fermi National Accelerator Laboratory, Batavia, Illinois 60510*
[e]*Laboratori Nazionali di Frascati, Istituto Nazionale di Fisica Nucleare, Frascati, Italy*
[f]*Harvard University, Cambridge, Massachusetts 02138*
[g]*University of Illinois, Urbana, Illinois 61801*
[h]*National Laboratory for High Energy Physics (KEK), Tsukuba, Ibaraki 305, Japan*
[i]*Lawrence Berkeley Laboratory, Berkeley, California 94720*
[j]*University of Pennsylvania, Philadelphia, Pennsylvania 19104*
[k]*Istituto Nazionale di Fisica Nucleare, University and Scuola Normale Superiore of Pisa, I-56100 Pisa, Italy*
[l]*Purdue University, West Lafayette, Indiana 47907*
[m]*Rockefeller University, New York, New York 10021*
[n]*Rutgers University, Piscataway, New Jersey 08854*
[o]*Texas A&M University, College Station, Texas 77843*
[p]*University of Tsukuba, Tsukuba, Ibaraki 305, Japan*
[q]*Tufts University, Medford, Massachusetts 02155*
[r]*University of Wisconsin, Madison, Wisconsin 53706*

(Received 13 August 1990)

We have determined $m_W = 79.91 \pm 0.39$ GeV/c^2 from an analysis of $W \rightarrow e\nu$ and $W \rightarrow \mu\nu$ data from the Collider Detector at Fermilab in $\bar{p}p$ collisions at $\sqrt{s} = 1.8$ TeV. From this result and the world-average Z mass, the weak mixing angle is determined to be $\sin^2\theta_W = 0.232 \pm 0.008$. An upper bound on the top-quark mass derived from this result is discussed.

I. INTRODUCTION

The unification of electromagnetic and weak interactions[1-3] is one of the most important landmarks in the understanding of the fundamental nature of matter. The masses of the intermediate vector bosons W and Z are fundamental to the standard model. Their ratio yields a measurement of the weak mixing parameter $\sin^2\theta_W$ which can be compared to determinations made using other methods, thus testing the consistency of the model.

Measurements of the W and Z masses have come from the CERN $\bar{p}p$ collider program.[4,5] More recently, accurate Z mass measurements made by the Collider Detector at Fermilab[6] (CDF) and the SLAC Linear Collider[7] (SLC) have been surpassed by those at the CERN e^+e^- collider LEP.[8-11]

We describe here a measurement of the W mass using the CDF at the Tevatron. A large sample of W bosons was recorded in an exposure of 4.4 pb^{-1} of 1.8-TeV $\bar{p}p$ collisions. The W mass is measured using both electron and muon decays of the W.

In Sec. II we describe the CDF and the triggers used to collect the W samples. The initial selections of the electron and muon data samples are outlined in Sec. III. The detector calibration necessary for measuring the W mass is detailed in Secs. IV and V. In Sec. VI the final selection criteria for the W mass samples are described. The procedure used to extract the W mass is described in Sec. VII. The simulation of W decay and detection along with the systematic uncertainties this introduces in the mass measurement are detailed in Sec. VIII. The measurement is summarized in Sec. IX, and the implications are discussed in Sec. X.

II. DETECTOR AND DATA COLLECTION

The CDF is a 5000-ton detector built to study $\bar{p}p$ collisions.[12] A quarter section is shown in Fig. 1. The CDF coordinate system defines the positive z axis along the direction traveled by the protons. The y axis is vertically upward and the x axis is radially outward from the center of the Tevatron ring. The angles θ and ϕ are the usual polar and azimuthal angles. Pseudorapidity, $\eta = -\ln\tan(\theta/2)$, is the polar angle variable appropriate for longitudinal phase space. The solenoid provides a magnetic field of 1.4116 T for magnetic analysis of charged particles in the central region ($40° < \theta < 140°$). Calorimeter coverage extends to within 2° of the beam line ($2° < \theta < 178°$, $-4.2 < \eta < 4.2$).

A. Tracking detectors

A vertex time-projection chamber system[13] (VTPC) surrounds the beam pipe and extends ± 1.4 m along the

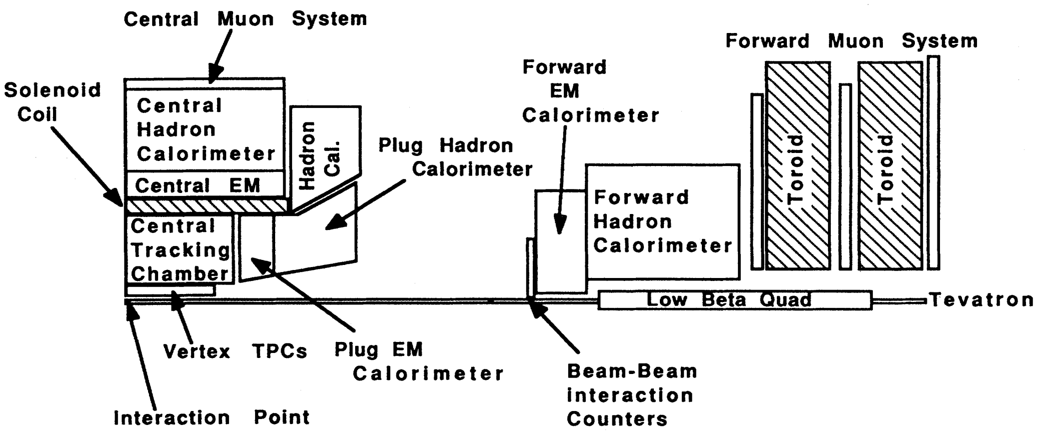

FIG. 1. CDF as configured during the running. Closest to the interaction point (at the far left) are the VTPC's, surrounded by the CTC, the solenoid coil, central EM and hadron calorimeters, and the central muon chambers. To the right are forward gas calorimeters and muon toroids.

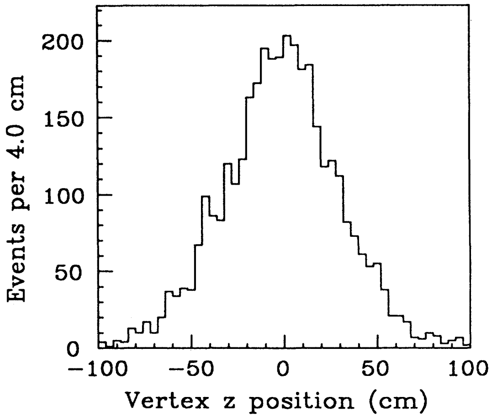

FIG. 2. Event vertex distribution along the beam line for the inclusive W decay to electron candidates. The distribution for the inclusive W decay to muon candidates is similar. In the final event sample, we require $|z| \leq 60$ cm.

beam line from the interaction point. This chamber measures charged-particle tracks in the r-z plane to within 3.5° of the beam line. The interaction vertex of the $p\bar{p}$ collisions is reconstructed with an rms resolution of 1 mm in the z direction. This vertex is used as the origin in computing the transverse energy ($E_T = E \sin\theta$) deposited in each calorimeter cell. The distribution in z of reconstructed vertices in candidate W events is shown in Fig. 2 and is well described as a Gaussian of mean −1 cm and width 31 cm. This spread in vertices reflects the convolution of the proton and antiproton bunches in the collider.

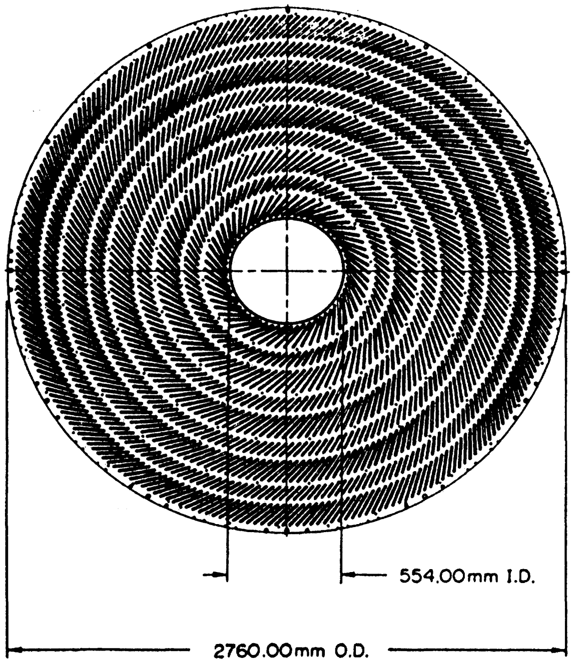

FIG. 3. Layout of wires at the end of the central tracking chamber (CTC) showing the grouping into nine superlayers and the 45° Lorentz angle.

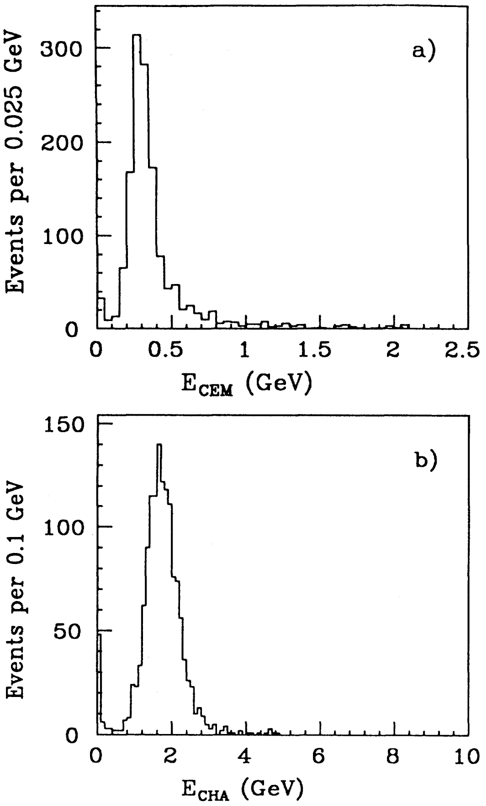

FIG. 4. Energy deposited in CEM and CHA by muons from J/ψ dimuon candidates. An invariant-mass plot for these candidates is shown in Fig. 11. The energy deposition is consistent with that seen in test-beam studies.

The central tracking chamber[14] (CTC) surrounds the VTPC. The CTC was designed to measure charged-particle tracks in the r-ϕ plane to determine their curvature in the magnetic field and thus their momenta. The CTC has 84 layers of wires grouped together in nine "superlayers" (see Fig. 3). The nine superlayers are subdivided into measurement cells. Five superlayers have 12 sense wires per cell, parallel to the beam direction. These axial layers are used for the primary determination of the track curvature. In the other four superlayers, each cell has six sense wires with a 3° stereo angle to provide information necessary to determine the polar angle of the tracks. The cells in all superlayers are tilted at a 45° angle with respect to the radial direction to compensate for the Lorentz angle of electron drift in the magnetic field. This allows the electrons to drift azimuthally (in the ideal case), simplifying the time-to-distance relationship.

The rms momentum resolution of the CTC is $\delta p_T / p_T = 0.0020 p_T$ (p_T in GeV/c) for isolated tracks. The addition of a requirement that a track intersect the beam at the beam position point (beam constraint) extends the effective tracking radius l from 1 to 1.3 m, thereby improving the effective resolution (which scales as $1/\beta l^2$) to $\delta p_T / p_T = 0.0011 p_T$. Complete tracking information is only available for $40° < \theta < 140°$. Tracks outside this angular region do not pass through all layers of the chamber and consequently have a poorer momentum resolution.

Muon chambers[15] are located behind the central calorimeters at a radius of 3.47 m. There are approximately five hadronic absorption lengths of material between the muon chambers and the interaction point. The chambers cover the rapidity region $|\eta| < 0.63$ $(56° < \theta < 124°)$. There is a gap between neighboring chambers at the boundary at $\eta = 0$ of about $\delta\eta = 0.05$. A 2.4° gap in ϕ between adjacent 15° calirometer sections also is not covered. The four layers of drift cells in a muon chamber provide three-dimensional reconstruction of tracks via single-hit time-to-digital converters (TDC's) in the transverse direction and charge division in the longitudinal direction. A drift resolution of 250 μm (ϕ) and a charge-division resolution of 1.2 mm (z) are determined from cosmic-ray studies.

Figure 4 shows the distribution of energy deposited in the central calorimeter by muons from candidate J/ψ decays. This distribution is similar to that obtained in a 57-GeV/c muon test beam. The average energy deposited is 0.3 GeV in the electromagnetic calorimeter (CEM) and 2.0 GeV in the hadronic calorimeter (CHA).

B. Calorimeters

The CDF has three calorimeter systems: central, plug, and forward (see Fig. 1). The central $(-1.1 < \eta < 1.1)$ system is made up of lead-scintillator shower counters (CEM) followed by an iron-scintillator hadron calorimeter. The active elements of the calorimeters outside the central region are gas-proportional chambers with cathode pad readout. The plug electromagnetic and hadronic calorimeters cover $1.1 < |\eta| < 2.4$, and the forward electromagnetic and hadronic calorimeters cover $2.2 < |\eta| < 4.2$.

The central electromagnetic calorimeter[16] (CEM) is used to measure the energy of the decay electron in the *W* decays in this analysis. It consists of 31 layers of polystyrene scintillator interleaved with 30 layers of lead absorber. Including the outer chamber wall, magnet coil, and the calorimeter itself, there are 19 radiation lengths of material. The central calorimeter is composed of 15° wedges in ϕ (see Fig. 5). Light from the scintillators is read out through wavelength shifters on both sides of a wedge in projective slices (cells) of the caloirmeter that cover 0.1 units of η per cell. Proportional chambers with fine-grained (1.5-cm spacing) strip and wire readout are located at a depth of 6 radiation lengths. The positions of

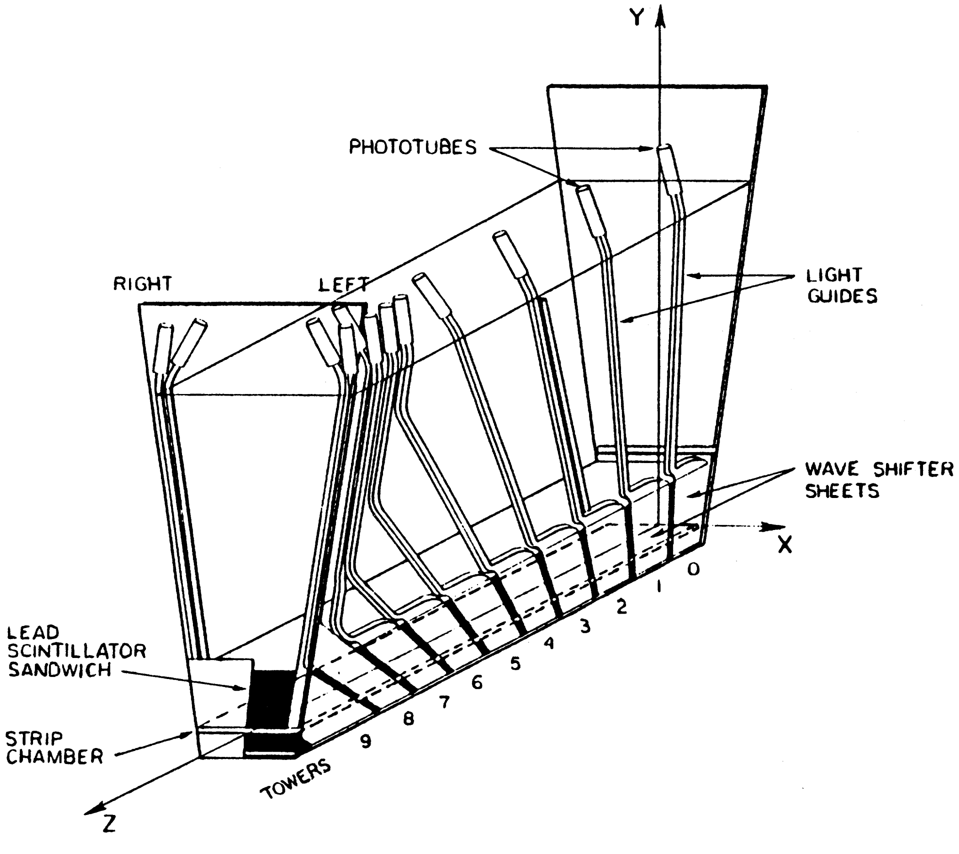

FIG. 5. Cutaway view of a central electromagnetic calorimeter module. The wavelength shifters collect the light from the layers of scintillators and indicate the cell structure in η. Each wedge subtends 15° in ϕ.

electron showers are measured with 3-mm accuracy with these chambers.

The energy scale used in triggering for each of the 478 CEM cells was defined by 50-GeV electrons in a test beam and has been maintained by ^{137}Cs sources.[17] All six CDF calorimeter systems are used to the infer the transverse energy of the neutrino coming from W decay. Each of these calorimeters used calibrations derived from studies in test beams with electrons and pions. We have checked the gas electromagnetic calorimeter energy scales with electrons from W and Z decay. The hadron calorimeters' response was checked with jet data.[18] In addition, we have studied the overall calorimeter performance in minimum-bias events, i.e., data taken with a minimal interaction trigger (see below). The detector response to these events should be similar to the response to the underlying event (the cylindrically symmetric component of the particles other than the W itself) in W production events.

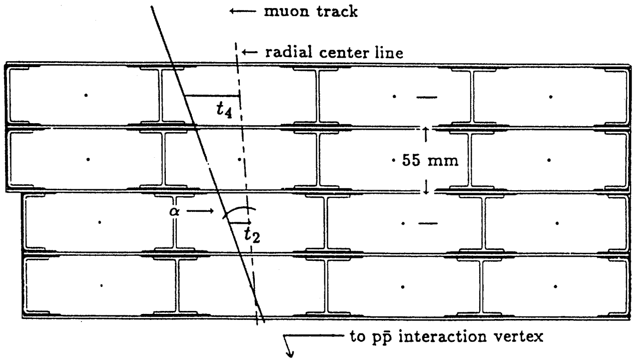

FIG. 6. Cross section of a muon chamber. Note the incident muon with an angle α and its associated drift times in two of the four layers.

C. Trigger

The interaction rate during the running at the Tevatron collider was 10^5 times higher than the CDF data-recording capability. To reduce the interaction rate to a rate that could be written to tape, we used a four-level trigger system.[19] A description of the triggers relevant to the collection of W candidates follows.

The lowest level of the triggering scheme, level-0, selected inelastic collisions by requiring that time-of-flight counters on either side of the interaction region (see Fig. 1) be hit in coincidence. This is the minimum-bias trigger. This trigger decision was available in time to inhibit data taking during the next beam crossing, 3.5 μs later.

The level-1 decision was made within the 7 μs allowed by level-0. If the event failed in level-1, the front-end electronics were reset in time for the second crossing after the initial level-0 decision.

The level-1 calorimeter trigger system[19] computed the energy flow in both the electromagnetic and hadronic compartments of the calorimeter. For W electron candidates, all events were required to have at least 6 GeV in a single trigger cell of the central electromagnetic calorimeter. A trigger cell combines two cells of the central calorimeter in the same wedge and is therefore 0.2 in η by 15° in ϕ.

The level-1 muon trigger used hits from the muon TDC's to identify high p_T track "stubs" in the muon chambers. The trigger imposed a cut on the time difference $|t_4-t_2|$ or $|t_3-t_1|$ (see Fig. 6) between two radially aligned wires in a muon tower, where t_i is the drift time to the ith wire in a muon tower.[20] This restricted the maximum allowed angle of a track with respect to an infinite-momentum track emanating from the $p\bar{p}$ vertex and thus applied a cut on the p_T of the track. Multiple scattering softens the trigger threshold in track p_T. Approximately two-thirds of the data set used in this analysis was gathered with a p_T threshold of 3 GeV/c, while the other third, taken early in the run, had a threshold of 5 GeV/c. A measurement of the trigger efficiency using cosmic rays shows that the efficiency for muon track finding in level-1 in either case is above 90% and is independent of p_T for tracks with transverse momentum greater than 15 GeV/c (see Fig. 7). Either wire pair of each muon tower can generate a level-1 trigger.

In level-2, both the electron and muon triggers (as well as other triggers) used two-dimensional tracks found by the central fast tracker (CFT), a hardware track processor[21] which used fast timing information from the CTC to detect high-transverse-momentum tracks. The track finder analyzed prompt hits from the axial sense wires of the CTC to identify tracks by comparing the hits in the CTC to predetermined hit patterns for the range of transverse momenta allowed by the CFT trigger threshold. The processor covered the p_T range from 2.5 to 15 GeV/c with a momentum resolution of $\delta p_T/p_T^2=3.5\%$ (where p_T is in GeV/c). The list of tracks found was presented to the rest of the CDF trigger system for use in

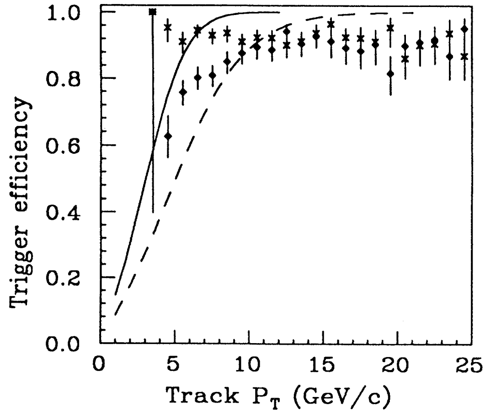

FIG. 7. Efficiency of the muon level-1 trigger as a function of track p_T. The efficiencies for both the 3 (×) and 5 GeV/c (◇) thresholds are plotted. The solid and dashed lines show predictions which include multiple scattering for the 3- and 5-GeV/c thresholds, respectively, but not the loss due to δ rays (Ref. 46).

level-2 decisions. The level-2 muon selection imposed a nominal 6-GeV/c threshold for tracks. The efficiency for finding tracks above 25 GeV/c was 98%, independent of track density in the event (see Fig. 8).

The level-2 trigger selected central electrons if (1) a cluster of transverse energy (see Ref. 22) was found with 12 GeV or more, (2) a track found by the CFT, with nominal threshold $p_T > 6$ GeV/c, pointed toward the wedge containing the cluster, and (3) less than 12.5% of the energy in the cluster was in the hadron compartments. By studying events passing other triggers, we found this trigger to be 98% efficient for W electrons. Comparisons of this trigger to lower-threshold electron triggers revealed that it was fully efficient for transverse energy above 15 GeV.[23,24] In this analysis we will only study electrons with $E_T > 25$ GeV.

The level-2 muon trigger[25] matched the list of tracks found by the CFT to stubs found by the muon level-1 trigger using lookup tables which took into account multiple scattering. These tables were stored in read-only memory (RAM). The p_T and ϕ for CFT tracks which had a match were then passed to the rest of the level-2 trigger system.

The data sample used in the muon analysis was selected by requiring only a match between a stub in a muon tower and a CFT track. No calorimeter information was used.

A level-3 trigger system[26] was also implemented during the running period. This consisted of a "farm" of 60 Motorola 68020 processors. All of the data for each event were available for each trigger decision. Because of the constraints on execution time per event, we used streamlined versions of the complete CDF reconstruction code.

The level-3 electron filter required that the electron cluster that was identified in level-2 have at least 12 GeV as reconstructed in software.[27] The filter also required that the fast reconstruction find a track of at least 6 GeV/c associated with the cluster.

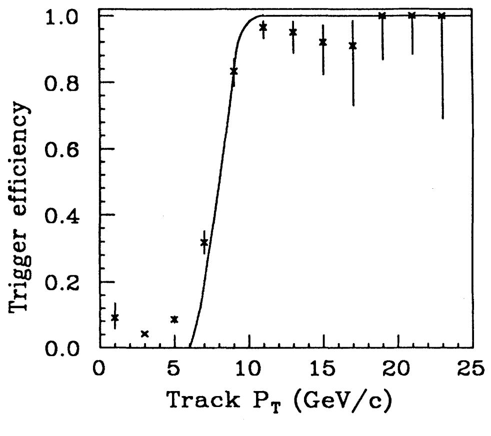

FIG. 8. CFT efficiency as a function of track p_T. The solid line is the nominal efficiency for the threshold used. The plotted points are the trigger efficiency for muon level-2 (CFT convolved with an assumed matching efficiency to the muon chambers of 100%) from muon data.

The fast, two-dimensional track reconstruction algorithm determined the p_T and ϕ of tracks at the radius of the muon chambers. Tracks above the level-3 p_T threshold of 9 GeV/c were matched to stubs identified by the muon level-1 trigger electronics within a 5° window in ϕ. If no match was found, the event was rejected.

D. Data collection

We collected the data used in this analysis over a 12-month period. The peak machine luminosity grew to over 2×10^{30} cm^{-2} s^{-1}. The overall trigger rate was limited to 1–2 Hz by the speed with which we could transfer data to tape. The average event record contained 120 kbytes of information. Our final 4.4-pb^{-1} sample consists of 4×10^{6} events recorded on 5500 magnetic tapes. The muon sample contains only 3.9 pb^{-1} because of a malfunction of the muon trigger during the early part of the run.

III. EVENT SELECTION

In this section we describe the selection criteria used to obtain the initial data samples used in determining the W mass. W and Z decays are the primary source of charged leptons with transverse momenta above 20 GeV. Furthermore, the neutrino from W decay escapes the detector, producing an apparent transverse-energy-flow imbalance. We isolate W decays by looking for high-transverse-momentum electrons with large missing energy or by looking for muons.

A. Electron event selection

We base our electron event selection on the missing-transverse-energy ($\not{E}_T$) signature for $W\rightarrow e\nu$ decays. The neutrino transverse energy is determined by measuring the net transverse energy imbalance in an event. We do this by constructing the vector

$$\mathbf{E}_T = \sum_i E_{T_i}\hat{\mathbf{n}}_i \,, \qquad (1)$$

where the sum is over all cells of the calorimeter and the $\hat{\mathbf{n}}_i$ are two-dimensional unit vectors pointing from the event vertex to the cell centers. The neutrino (vector) transverse energy is then given by $\not{\mathbf{E}}_T = -\mathbf{E}_T$. Because the low-$\beta$ quadrupole magnets obscure part of the forward hadron calorimeter, the sum in Eq. (1) is limited to those cells with $|\eta| < 3.6$. To be included in the sum, individual cell energies (not transverse energies) must exceed detector-dependent energy thresholds. These thresholds are 100 MeV in the central electromagnetic and hadronic cells, 300 MeV in the plug electromagnetic calorimeter, 500 MeV in the plug hadronic and forward electromagnetic calorimeters, and 800 MeV in the forward hadron calorimeter.

We reconstruct the calorimeter transverse energy in data events and require (1) that $|\not{\mathbf{E}}_T|$ be greater than 20 GeV. We further require (2) that the $\not{\mathbf{E}}_T$ significance ($S \equiv |\not{\mathbf{E}}_T|/\sqrt{\sum E_T}$) be greater than 2.4 GeV$^{1/2}$, which is a cut of more than 4σ in minimum-bias events which should be azimuthally symmetric. Here the $\sum E_T$ refers to the scalar sum of all transverse energy observed in the event using the above tower thresholds and η range. This cut helps eliminate poorly measured jet events. It is essentially irrelevant for the clean $W \rightarrow e\nu$ topology (see Fig. 9). We select electrons by requiring (3) that the events have one or more clusters of energy with E_T greater than 15 GeV. Our (jet) clustering algorithm starts with a single calorimeter seed cell with E_T greater than 3 GeV. It then adds all cells within a cone of 0.7 [opening angle$=(\Delta\eta^2+\Delta\phi^2)^{1/2}$] having energy greater than 0.1 GeV, computing the energy weighted centroid of the cluster. The procedure iterates (starting with the cone centroid rather than the seed cell) grouping energy inside a cone of 0.7 until the centroid stabilizes. Further details can be found in Ref. 28. We also require (4) that the leading (highest E_T) cluster has at least 5% of its energy in the electromagnetic calorimeter; this avoids unphysical events with all the energy deposited in the hadron calorimeter. Finally, we require (5) that there be no cluster with $E_T \geq 5.0$ GeV opposite the leading one, within 30° of azimuth. This reduces the residual dijet background. Even when mismeasured, dijet events generally leave some jet activity opposite the leading cluster of energy.

These requirements give a factor of 60 reduction from our initial data sample; we are left with 65 000 events from 4.4 pb^{-1}. A Monte Carlo estimate shows that this procedure has an 80% efficiency for selecting W candidates that leave an electron in the central detector.[29]

To isolate a clean W sample from the inclusive $\not\!\!E_T$ data sample described above, we make additional requirements on the electron. These requirements are as follows. We require (6) that the highest-energy cluster, which corresponds to the electron, be located in the central detector ($|\eta| \leq 1.0$), (7) that the fraction of the cluster energy in the electromagnetic compartment be greater than 85%, and (8) that a track of momentum p point at the cluster with $E/p \leq 2$, where E is the energy of the cluster.

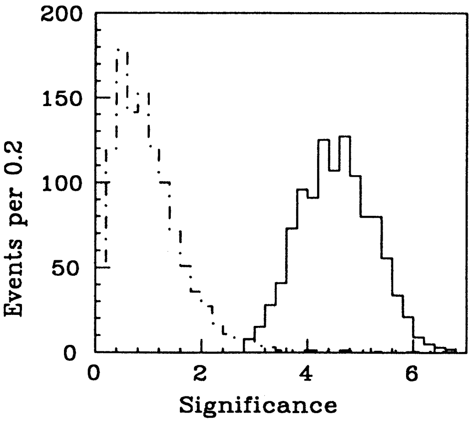

FIG. 9. $\not\!\!E_T$ significance (described in the text) for a sample of dijet events (dotted histogram) and our W sample (solid histogram). The normalization of the dijet sample is arbitrary.

An inclusive central W electron sample of 3350 events remains after these requirements are met.

B. Muon event selection

Our first pass selection of muon candidates cuts only on quantities associated with the muon. The same fast, two-dimensional track-reconstruction algorithm used in the level-3 trigger is used to select events containing a track with transverse momentum above 20 GeV/c. These events are then completely reconstructed, and events containing a muon with $p_T \geq 20$ GeV/c that deposited less than 2 GeV of energy in the electromagnetic calorimeter and less than 6 GeV in the hadronic calorimeter are kept for further analysis. These requirements result in a sample of 10 385 events. Selection requirements for the final mass samples will be discussed in Sec. VI.

IV. CHARGED-LEPTON MEASUREMENT CALIBRATIONS

A. Muons

The most important calibration for W decays to muons is that of the central tracking chamber. It is there that we measure the muon p_T. Calibration of the muon chambers themselves enters only in our ability to match tracks in the muon chamber with the extrapolated CTC track. We first discuss calibration of the muon chambers and readout electronics before taking up calibration of the tracking chamber.

Calibration of the muon chambers is straightforward. The relative timing between channels is determined by pulsing the sense wires. The global timing is fixed by comparing the earliest hit distribution with the beam-beam crossing time. The drift velocity is monitored by comparing the drift-time differences between alternate layer sense wires which are offset by 2 mm. The charge division coordinate is calibrated using signals from ^{55}Fe sources located inside the chambers. Survey information is used to fix the muon chamber positions relative to the beam interaction region. Finally, the matching of CTC tracks to muon stubs serves as an overall check. Figure 10 shows the distribution of differences of extrapolated CTC tracks and muon stubs. The distribution is consistent with multiple scattering.

Calibration of the CTC begins with pulsers used to determine relative timing between channels. The determination of timing offsets, drift parameters, and a beam position is performed on a run-by-run basis. We determine the chamber alignment parameters by using charged-particle tracks in minimum-bias events. The tilted geometry of the drift-chamber cells means that each track provides a measurement of the drift-time relationship. These calibration constants are calculated on line and are available for the first pass reconstruction. Having reconstructed tracks with this alignment, we find average axial residuals of 180 μm and average stereo residuals of 225 μm. The beam center is determined with 5-μm accuracy for a (typical) 50-μm beam size.

Remaining tracking chamber distortions fall into two

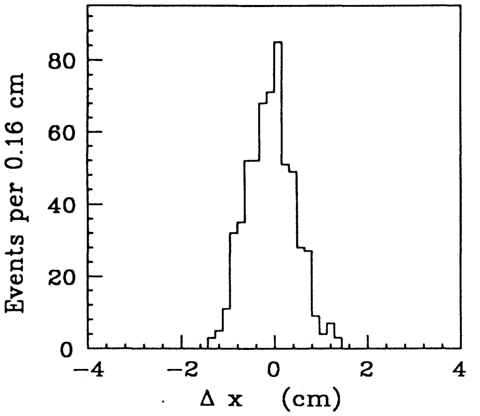

FIG. 10. Match between the CTC track extrapolated to the lowest wire plane of the muon chambers and the muon chamber track at that point (R-ϕ plane). $X=0$ is defined to be the midpoint of the muon chambers in the calorimeter wedge.

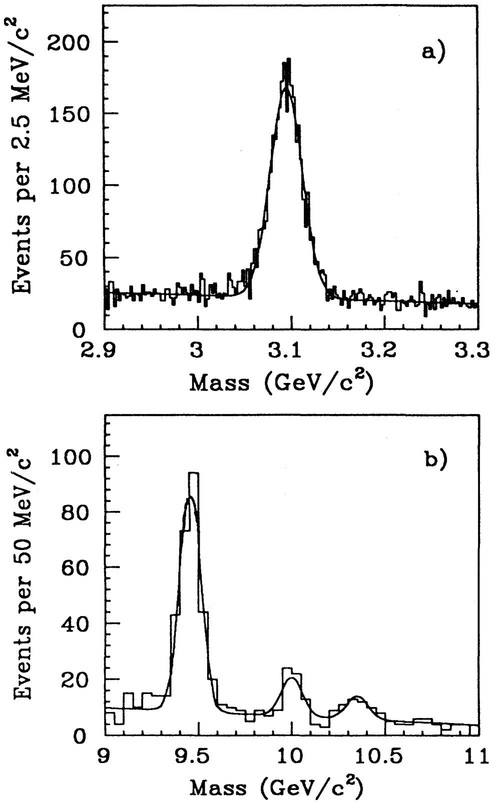

FIG. 11. (a) Invariant-mass distribution of a sample of J/ψ dimuons and (b) a sample of Υ dimuons which we use as a check of the tracking chambers's momentum scale. From the agreement between the CDF measured masses and the world-average masses, we conclude that the tracking chamber is absolutely calibrated to 0.1%. The curves correspond to a Gaussian-plus-second-order-polynomial background fit to the data with the width a free parameter.

categories: (1) overall magnification due, for example, to mechanical loading and (2) azimuthal misalignments. An overall dilatation of the chamber is equivalent to an error in the magnetic-field strength. The nominal wire locations are surveyed with a precision of 50 μm, and the absolute magnetic field is mapped to ±0.05%. We check for residual chamber dilatations using samples of J/ψ and Υ dimuons (see Fig. 11). Compared to the Particle Data Group (PDG) values,[30] both the J/ψ mass and the Υ mass are correctly determined, 3.0963 ± 0.0005 (CDF) versus 3.0969 ± 0.0001 (PDG) and 9.457 ± 0.005 (CDF) versus 9.4603 ± 0.0002 GeV/c^2 (PDG), respectively. Muon transverse momenta in these samples are typically 5–6 GeV/c. We conclude that the tracking chamber momentum scale is known to at least 0.1%, averaged over charges.

The other concern is azimuthal alignment errors which can effect the chamber's resolution at high momenta by leading to charge-dependent sagitta errors of the type

$$\frac{1}{p}=\frac{1}{p_{\text{true}}}+\frac{1}{\Lambda}\quad (e^+,\mu^+)\,, \tag{2}$$

$$\frac{1}{p}=\frac{1}{p_{\text{true}}}-\frac{1}{\Lambda}\quad (e^-,\mu^-)\,, \tag{3}$$

where Λ is a false momentum. By comparing average energy-to-momentum ratios $\langle E/p\rangle$ for electrons and positrons, we get

$$\frac{1}{\Lambda}=\frac{1}{\langle E\rangle_+ + \langle E\rangle_-}(\langle E/p\rangle_+ - \langle E/p\rangle_-)\,. \tag{4}$$

By equalizing $\langle E/p\rangle$ for electrons and positrons and requiring that they emanate from a common beam spot, we determine 166 wire-layer azimuth offsets (one for each wire layer at each end of the chamber less two overall phases). The sign-dependent shifts are 3% before the alignment correction for a 35-GeV/c track and are less than 0.2% after. Such a shift has a negligible effect on the statistically charge-symmetric samples of the size being considered. We also correct for the effect of gravity on the chamber wires. We use cosmic rays, which provide apparent tracks of equal momenta but opposite charge, to verify the alignment. Figure 12 shows the improvement in curvature matching of cosmic-ray branches after the alignment. The alignment does not change the scale; it only improves the resolution at high momentum. When the beam position is included in the track fit, the chamber resolution is $\delta p_T/p_T=0.0011p_T$ (p_T in GeV/c) or about 1.3 GeV/c for the 35-GeV/c tracks typical of W decay leptons.

As a check of the tracking chamber calibration, we compare the Z mass we measure[6] with our $Z^0\to\mu^+\mu^-$ sample to the world average, which is dominated by the LEP measurements. Our result is $m_Z(\mu\mu)=90.71\pm0.45$ GeV/c^2. The PDG average[30] is $m_Z=91.161\pm0.031$ GeV/c^2. These are in good agreement.

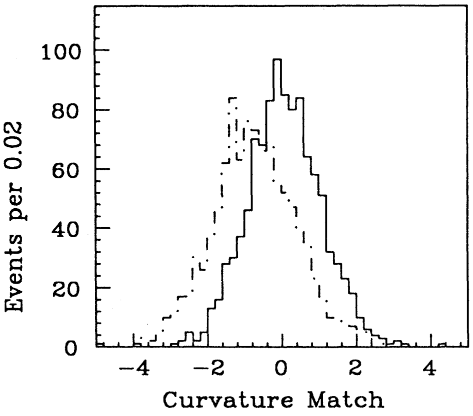

FIG. 12. Difference in curvature between the incoming and outgoing branches of a cosmic ray. These branches leave tracks of equal, but opposite signed curvature. The solid (dotted) histogram shows the matching after (before) chamber alignment. The matching is normalized to the curvature uncertainties and thus should have mean 0.0 and σ 1.0. The residual charge asymmetry corresponds to an 0.3% difference in momentum for a 35-GeV/c track.

B. Electron calibration

Having verified the momentum scale of the CTC, we use it to determine the energy scale of the calorimeter. Electron showers in the central calorimeter may span several calorimeter cells in a single wedge. For a cluster (as found by our algorithm) to expand beyond one cell, a neighboring cell must have more than 100 MeV of E_T. We use the two highest-energy adjacent cells of the electromagnetic calorimeter to compute an electron energy. A response map for each cell, determined in the test beam,[31] gives a correction based on the shower position measured by the strip chambers. This correction accounts for light attenuation, the effect of cracks, and transverse shower leakage, and is accurate to ±1% over the fiducial area we use, defined below.

Calorimeter cell-to-cell variations can lead to offsets of the form

$$E_i = E_{\text{true}}(1+\epsilon_i) \ . \tag{5}$$

Here the offsets ϵ are common to electrons and positrons. We equalize the gains in individual calorimeter cells using a sample of inclusive electrons with $E_T > 15$ GeV. In order to select the sample of inclusive electrons, we require the fraction of the electron candidate's energy leaking into the hadron calorimeter compared to the energy in the electromagnetic calorimeter be less than 0.04, the energy sharing among cells in the cluster be consistent with that observed in the test beam, the shower profile seen in the strip chamber be consistent with test-beam showers ($\chi^2/N_{\text{DF}} < 10$ for 9 degrees of freedom in each view), and the CTC track and shower positions match within $\delta x \leq 1$ cm and $\delta z \sin\theta \leq 8$ mm. These distributions are shown for the electrons from the W sample in Fig. 13; no selection on these variables was made for this sample. We further require $0.7 \leq E/p \leq 1.3$ (see Fig. 14), and the pulse-height ratio of wires to strips of the strip chamber be within 40% of the nominal. This results in the selection of 17 000 electron candidates, about 35 per tower. The selection is not highly restrictive, leaving about 4% background. This background can shift the mean E/p, but it influences all cells similarly. The resulting relative cell gains have an average statistical accuracy of 1.7%. Figure 15 shows a distribution of the ratio of individual cell gains to those derived from test-beam calibrations.

The overall scale factor for the CEM energy comes from a comparison of E/p for W electrons to a prediction that includes radiative effects. The W sample provides a pure (>99%) sample of electrons. The calibration relies on the comparison of the measurement of the electron's energy in the calorimeter to the measurement of the electron's momentum in the tracking chamber. It is independent of the electron's kinematic distribution except for small calorimeter nonlinearities which will be discussed in Sec. X. We use the same fiducial region for both the calibration data and W mass data. We require that the centroid of the strip chamber shower associated with the electron be more than 1.5° away from central wedge boundaries, 12 cm from the calorimeter module separation at 90°, and 45 cm away from the central-plug boundary of the calorimeter. The average energy does not match the average momentum exactly, as high-energy electrons radiate in the detector, lowering the observed momentum. The W decay may also have associated internal radiation. While the calorimeter measures most of the radiated photon energy, the tracking chamber measures only the momentum of the charged track. Thus we expect $E/p \geq 1$ on average.

We fit the peak of the E/p distribution (see Fig. 16) to a Gaussian. Events in windows centered on the peak are fit using a log-likelihood method. A typical window is $0.90 < E/p < 1.12$. For our selection of windows, the simulation predicts shifts in the central value of the fit of less than 1% due to radiation. This technique is statistically more favorable and less sensitive to uncertainty in material than that of Ref. 6.

The size of the radiative tail is predicted from the nominal amount of material in the detector, or alternatively, it can be used as an empirical measure of the material. The radiative tail in the data is quantified as the mean E/p for all electrons with $E/p < 1.4$. The simulation predicts that this mean should be shifted by about 3%. A comparison of the peak shift and truncated mean shift in the simulated sample to the data indicates that the radiative tail in the simulation is a bit too large. For our final estimate of the material in the detector causing external radiation, we combine the material as accounted for in the simulation weighted by its uncertainty with an empirical determination from the radiative tail with its statistical uncertainty. The nominal peak shift of 0.94% predicted by the amount of material in the radiative simulation is reduced to 0.87%. The shift of the peak is assigned a systematic error of 0.10%, reflecting this uncertainty in material. Additional systematic uncertainty due to sensitivity to choice of fitting window, resolution, and

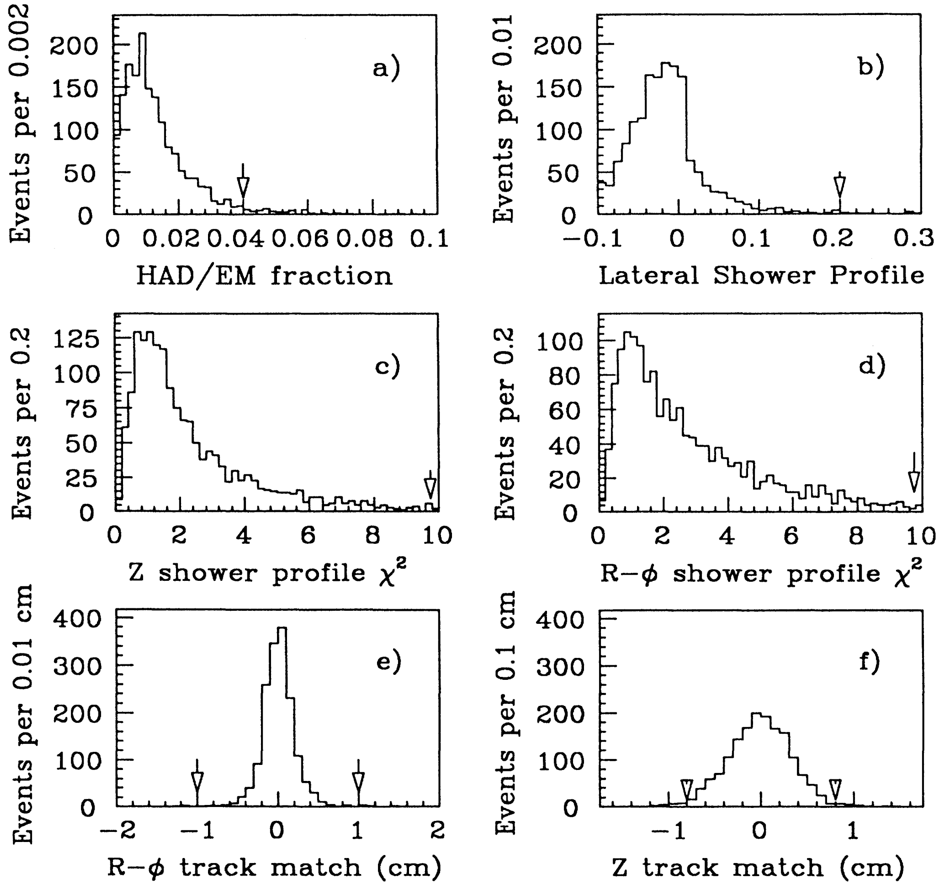

FIG. 13. Six different variables we use in the inclusive electron. The arrow in each figure shows the cut in each variable. We do not use these quantities to select the *W* mass sample. LSHR [in (b)] is the sum over the neighboring electron cells: $\sum [E_i(\mathrm{obs})-E_i(\mathrm{pred})]/\sigma$. The predictions, along with their uncertainties σ, come from test-beam measurements. We use distributions like these to determine the efficiency of these cuts when applied in other analysis (Refs. 23, 24, and 41).

data selection is 0.11%. The statistical uncertainty for this sample of 1700 *W* electron candidates is 0.16%. Thus we are left with an overall systematic uncertainty on the energy scale of

$$(0.10^2_{(\mathrm{tracking})}+0.16^2_{(\mathrm{stat})}+0.10^2_{(\mathrm{material})}+0.11^2_{(\mathrm{syst})})^{1/2} \qquad (6)$$

$$=0.24\% \ .$$

We consider one further complication. Some of the energy from the event underlying the *W* ends up in the same cell(s) as the electron being measured. We estimate this to be 50 MeV in each electromagnetic cell. This energy is included in the calibration. This definition creates a negligible nonlinearity (3×10^{-4}) in comparing *W*'s to *Z*'s.

We can check the calorimeter calibration by comparing the *Z* mass we measure in the calorimeter to that in the world average. Our calorimeter result from Ref. 6 is $m_Z(ee)=91.12\pm0.52$ GeV/c^2. If scaled up by 1.0028 for

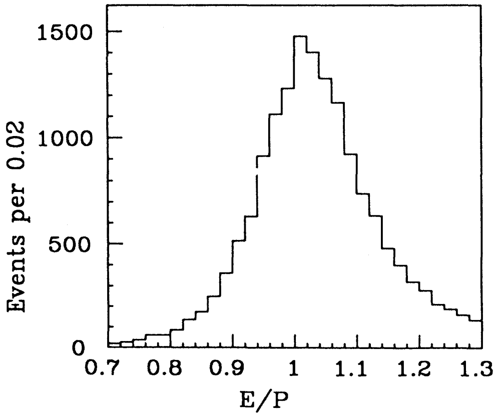

FIG. 14. *E/P* distribution for 17 000 inclusive electrons which we use to determine cell-to-cell relative normalization in the central electromagnetic calorimeter.

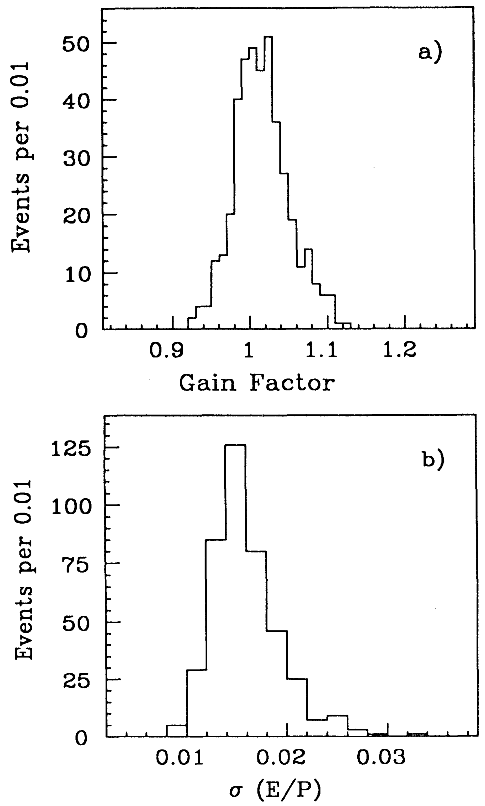

FIG. 15. (a) Cell-to-cell factors applied to the nominal test-beam gains maintained using sources. There is an overall shift of 1.7% in the average calibration of the calorimeter with a spread of 2.5%. (b) Statistical uncertainty on setting each of the cells. The average setting uncertainty of the individual cells is 1.7%.

the new energy scale used in this analysis, the value compares well with the PDG value[30] of 91.161±0.031 GeV/c^2.

V. NEUTRINO ENERGY CORRECTIONS

We use minimum-bias events taken during the course of normal data taking to study the $\not\!\!E_T$ response. There are overall offsets in $\not\!\!E_T$ due to residual pedestal and noise problems of −250±40 MeV in x and 100±40 MeV in y in the projections of the $\not\!\!E_T$ of these events as shown in Fig. 17. We correct for these average shifts in the reconstruction of the W events. The resolution in $\not\!\!E_T$ can be approximated by a constant times the square root of the total scalar E_T observed in the event (see Fig. 18):

$$\sigma(\not\!\!E_{x,y})=(0.47\pm0.03\ \mathrm{GeV}^{1/2})\left[\sum E_T\right]^{1/2}. \qquad (7)$$

This relationship applies before multiplicative corrections discussed below. Our model of W production consists, in part, of an uncorrelated underlying event that behaves similarly.

When measuring $\not\!\!E_T$ in an event with a charged lepton, we separate the charged lepton from the rest of the event. To avoid counting electron energy in the background event, we measure the electromagnetic and hadronic $\not\!\!E_T$ in all of the calorimeter except the three cells in η centered on the electron cluster. We expect the muon to deposit all of its energy in one calorimeter tower and re-

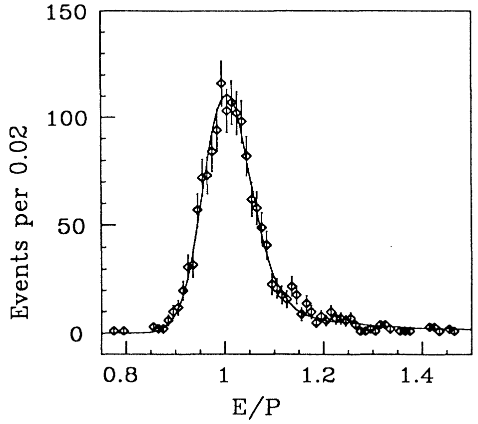

FIG. 16. E/P distribution for W decay electrons compared to the radiative simulation. This match sets the overall scale of the central electromagnetic calorimeter. The curve is the Monte Carlo prediction.

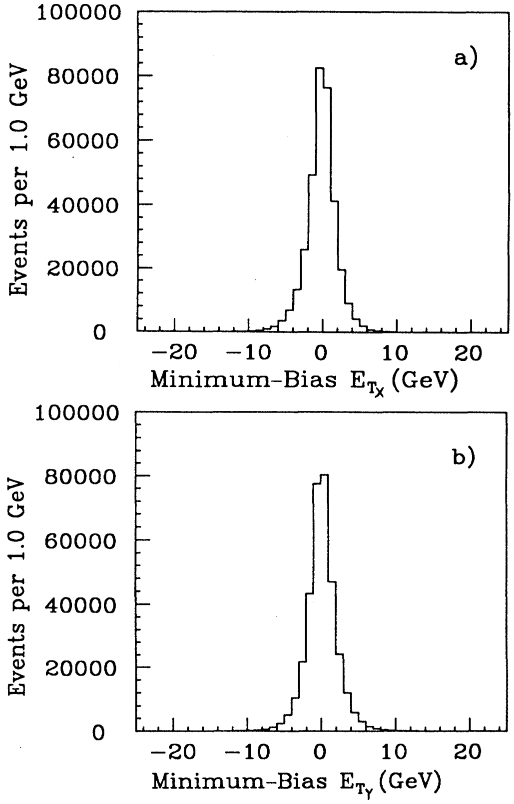

FIG. 17. (a) x projection of $\not\!\!E_T$ for 340 000 minimum-bias events. (b) y projection.

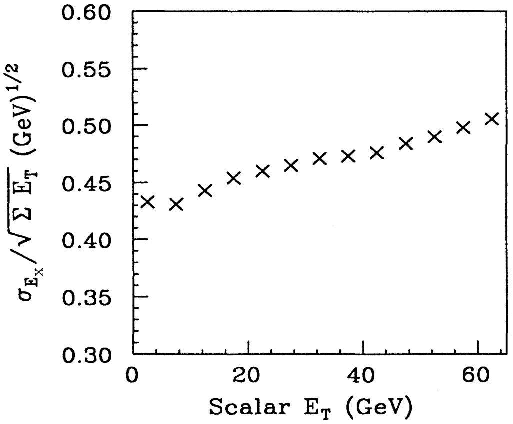

FIG. 18. Dependence of $S \equiv \not\!\!E_X/(\sum E_T)^{1/2}$, a neutrino-resolution variable, on the total scalar E_T observed in the event. This plot shows that the constant of proportionality between $\not\!\!E_x$ and $(\sum E_T)^{1/2}$ is 0.47 GeV$^{1/2}$ over the range of $\sum E_T$ covered by the *W* decay candidates (see Fig. 27). The residual $\sum E_T$ dependence of *S* has negligible effect on the *W* mass.

move only that tower from the computation of $\not\!\!\mathbf{E}_T$. We then define $\not{\mathbf{u}}$ to be the $\not\!\!\mathbf{E}_T$ of the event with the lepton effects nominally removed. The neutrino transverse momentum is then reconstructed as

$$\mathbf{v} = \not{\mathbf{u}} - \mathbf{p}_T^l \; , \tag{8}$$

where *l* refers to *e* or μ.

There are three additional corrections to be made. (1) Studies of the amount of energy deposited in central calorimeter cells away from the charged lepton in *W* events show that, for the 100-MeV single-tower energy threshold, an average of 20±2 MeV per cell of underlying event energy is lost in removing a cell. We correct $\not{\mathbf{u}}$ appropriately for electron and muon events. (2) In electron events, we find an average of 260±20 MeV of excess energy in the surrounding cells. This is consistent with expectations from transverse electron shower leakage. We partially correct $\not{\mathbf{u}}$ for this leakage and constrain the Monte Carlo model (see Sec. VIII) to reproduce its component along the charged-lepton direction ($\not{u}_\parallel$). Systematic uncertainties associated with these procedures are quite important since an error in $\not{\mathbf{u}}$ directly effects the *W* mass. We study these systematics by comparing the projections of $\not{\mathbf{u}}$ ($\not{u}_\parallel$ and $\not{u}_\perp$) parallel and perpendiuclar to the charged-lepton direction. (3) The response of the calorimeter to low-energy hadrons has been measured.[18] The calorimeter response to charged particles is shown as a function of momentum in Fig. 19. In order to compensate for calorimeter nonlinearities, we multiply $\not{\mathbf{u}}$ by a factor $k_u^0 = 1.4$. Associated systematics will be discussed in Secs. VIII and IX.

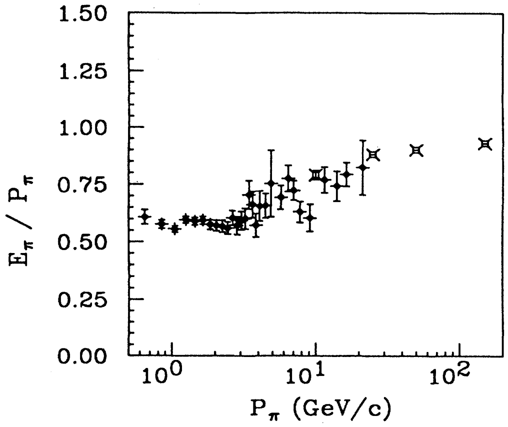

FIG. 19. Ratio of the energy observed in the combined hadronic and electromagnetic calorimeter using nominal test-beam calibrations compared to the track momentum for isolated charged pions. The response at low energies is depressed. The fragmentation of jets (into charged and neutral hadrons) is such that this falloff in response results in an undermeasurement of jet energies by a factor of approximately 1.4 for low-energy (30-GeV) jets.

VI. *W* MASS SAMPLE

The final samples for mass measurement involve further selections. For both samples, we require each lepton p_T (electron or muon and reconstructed neutrino) to be above 25 GeV/*c*. This reduces background with little loss to the mass information. To maintain calorimeter Hermeticity, we eliminate events with interaction vertices greater than 60 cm away from $z=0$. The calorimeter measurement of $\not\!\!E_T$ is a major component of the overall resolution. We restrict ourselves to more accurately measured, relatively clean events by requiring no calorimeter transverse-energy cluster, other than the one including the electron, above 7 GeV (before applying k_u^0). The distribution of cluster transverse energies for the electron sample is shown in Fig. 20. An alternative to this jet cut is discussed in Sec. IX.

The electron sample is restricted to the fiducial area used in determining the energy scale. The E/p ratio must be less than 1.4. Only one track may point to the electron seed tower. To remove mismeasured $Z \rightarrow ee$ events, no other track with $p_T > 15$ GeV/*c* may be present. The events that fail this cut are consistent with $Z \rightarrow ee$. Finally, we reject events in which the electron is part of a possible photon conversion pair, identified by either a soft opposite-sign track accompanying the electron or the absence of at least half the expected hits in the VTPC. Most of the detector material causing conversions is located at the outer radius of the VTPC. The conversion filter removes 3% of the events in the sample. This is consistent with no background, as the study of conversion candidates from regions with little or no material finds an accidental rejection of 3–4 %.

The muon sample is further refined by requiring no more than 3.5 GeV combined electromagnetic and hadronic energy be observed in the struck calorimeter tower (see Fig. 4). The muon track in the CTC is required to

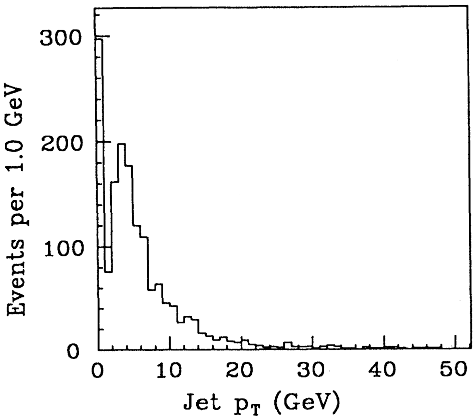

FIG. 20. Jet p_T (raw cluster) spectrum associated with W candidates. Attempting to measure extra partons (responsible for such jets) degrades the neutrino resolution. We remove all W candidates with associated jets above 7 GeV/c of p_T. Our jet clustering threshold is about 5 GeV; the spike at 0 represents W events where no jet cluster is found.

match the primary vertex of the event. The distance dx between the extrapolated CTC track and the muon stub is computed, and the requirement $|dx|<1.5$ cm is imposed as shown in Fig. 10. To reduce punchthrough background, the dijet cut as applied to the electron sample is applied to the muon sample (no cluster above 5 GeV within 30° back to back in ϕ with the muon). As in the electron sample, we reduce the background from $Z\rightarrow ll$ by allowing no other track with p_T greater than 15 GeV/c. This also eliminates the background from cosmic rays arriving in time with a $\bar{p}p$ collision. Additional cosmic rays are removed by rejecting events with a track of p_T greater than 10 GeV/c within 3° in ϕ of the direction opposite the muon or with a second muon stub consistent with a cosmic ray. The final samples contain 1130 electron candidates and 592 muon candidates.

VII. FITTING PROCEDURES

Unlike the measurement of the Z^0 mass, which is done by comparing the data to an analytic form, the measurement of the W mass relies on the comparison of the data to Monte Carlo line shapes for various kinematic quantities of the charged-lepton–neutrino system. We infer the neutrino p_T from the transverse-energy imbalance we observe in the detector; we cannot measure the longitudinal momentum of the neutrino. The Monte Carlo predictions include the physics of W decays as well as a simulation of detector response. We vary the W mass (and width) hypothesis in the simulation and compare the results to the data.

While the electron, muon, and neutrino p_T spectra from W decay display a Jacobian edge, it is smeared both by the poorly determined p_T of the parent W and by detector resolution. By combining the inferred measurement of the neutrino p_T with the charged lepton p_T, we limit the sensitivity of our measurement to the p_T of the W. We use the transverse mass of the charged-lepton–neutrino system to determine the W mass:

$$m_T=\{2p_T^l p_T^\nu[1-\cos(\phi^l-\phi^\nu)]\}^{1/2}\ , \tag{9}$$

where l labels the transverse momentum and azimuth of the electron or muon, and ν refers to the reconstructed neutrino. This is the three-dimensional analogue of the product of four-vectors that gives the invariant mass. The transverse-mass distribution for our final data samples is shown in Fig. 21. The upper edge of the transverse-mass distribution is kinematically constrained by the W mass and, thus, provides most of the information in the fits. The loss of energy into longitudinal motion can only reduce the observed transverse mass. We also study the charged-lepton and neutrino p_T spectra as a check of the details of our model.

We determine the mass of the W by fitting the transverse mass to Monte Carlo predictions with m_W and Γ_W as parameters, or with Γ_W constrained to 2.1 GeV, the value predicted by the standard model. The Monte Carlo model will be discussed in detail in Sec. VIII. We generate predictions for m_T, p_T^l, and p_T^ν for masses m_W between 77.8 and 82.3 GeV/c^2 in steps of 0.5 GeV/c^2 and widths Γ_W between 0.375 and 2.25 GeV in steps of 0.375 GeV and between 2.25 and 6.0 GeV in steps of 0.75 GeV. Roughly 10^6 W decays go into the prediction of the line

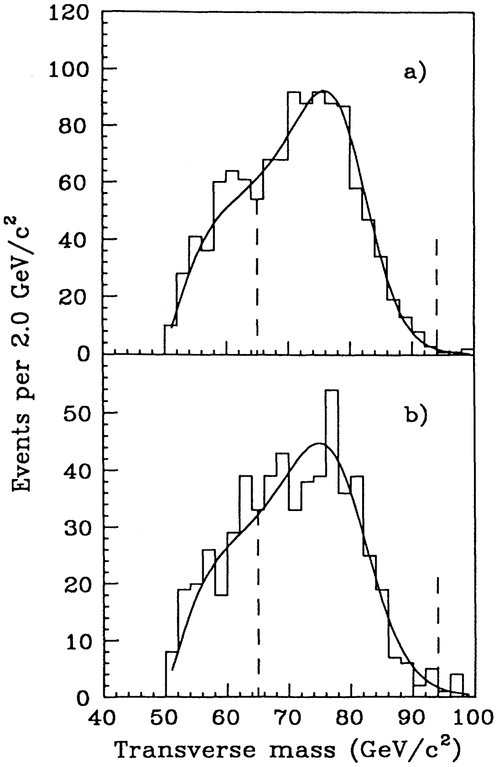

FIG. 21. (a) Transverse-mass distribution for all $W\rightarrow e\nu$ candidates. Overlaid is the best fit to the data. Indicated with dashes is the range of transverse mass used in the fit. (b) Transverse-mass distribution for all $W\rightarrow\mu\nu$ candidates.

shape for each mass-width combination. We store the distributions in 1-GeV/c^2 intervals of transverse mass, giving an m_T (or p_T^l, p_T^ν) probability distribution, $P(m_W, \Gamma_W)$.

There is a sensitivity to a correlation of the fluctuations of a relatively small sample the size of the data samples, 1130 and 592 events, and the larger Monte Carlo samples used for each value of mass and width in the fitting grid. This would be reflected in a fitting uncertainty of about 100 MeV/c^2. We reduce the effect of these fluctuations by smoothing the line shapes as follows. We parametrize the contours in m_W at constant m_T and Γ_W by a second-degree polynomial. These contours are plotted in Fig. 22 for $\Gamma_W = 2.25$ GeV/c. After this smoothing, there is a residual uncertainty of 50 MeV/c^2 which persists even when fitting very large Monte Carlo samples. We thus assign a 50-MeV/c^2 uncertainty due to the characteristics of the fitter.

We compare the simulated line shapes to the data using an event-by-event likelihood. We maximize the likelihood function

$$
\begin{aligned}
L &= \prod [P_i(m_W, \Gamma_W)] \ , \\
\ln L &= \sum \ln[P_i(m_W, \Gamma_W)] \ ,
\end{aligned}
\tag{10}
$$

as a function of mass and width with the MINUIT optimization package.[32] The product and sum extend over all events in our fitting range ($65 < m_T < 94$ GeV/c^2). Although we generate line shapes at discrete masses and widths, we interpolate in both directions to generate a prediction for any mass and width. Several methods of interpolation (bilinear, polynomial, bicubic, and bicubic spline[33]) give the same results. For our final results we use the bicubic spline, which consists of successive one-dimensional interpolations. At each of the four grid points surrounding the desired mass-width point, we specify the probability P, the derivative in each direction, $\partial P/\partial m_W$ and $\partial P/\partial \Gamma_W$, and the cross derivative $\partial^2 P/\partial m_W \partial \Gamma_W$. We determine the derivatives at the grid points with one-dimensional splines. We then use a cubic polynomial to find an interpolated value. This provides a continuous prediction in m_W and Γ_W.

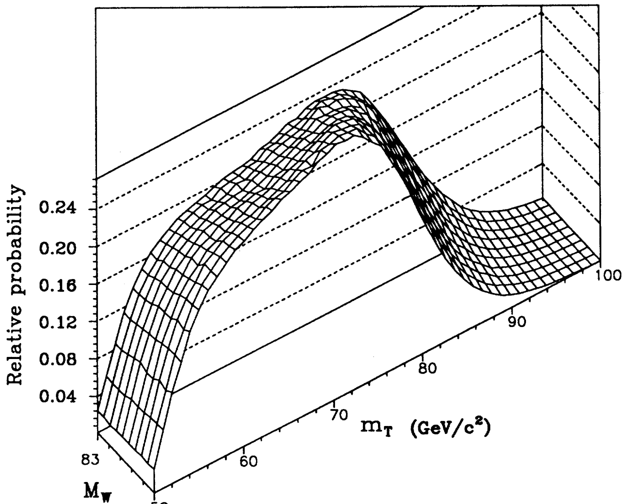

FIG. 22. Raw relative probability surface as a function of m_W and m_T for $\Gamma_W = 2.25$ GeV/c. The contours at constant m_T are then parametrized by second-degree polynomials. Masses are given in units of GeV/c^2.

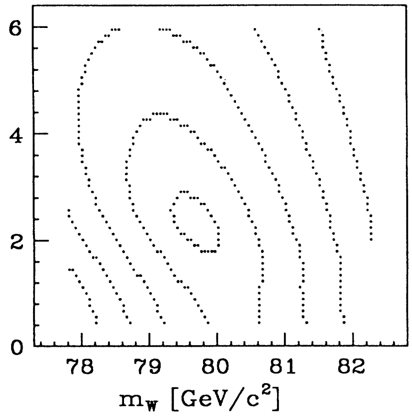

FIG. 23. Likelihood contours in mass and width showing the correlation between the mass and width. The electron sample is shown.

Once we have the line shape for a given mass and width, we compute the probability $P_i(m_W, \Gamma_W)$ that any individual event comes from this distribution by doing a linear interpolation between the nearest stored probabilities. A cubic spline interpolation gives identical results. We fit only the shape of the distribution and not the number of events. The statistical uncertainty will be further discussed in Sec. IX.

Figure 23 shows the coupling between the fit mass and width. MINUIT reports a 20–40 % correlation between these parameters. The detector resolution and fit width are highly correlated, which implies a correlation between the mass and detector resolution. This motivates the need to understood the detector resolution in making Monte Carlo predictions.

VIII. UNDERLYING EVENT MODEL AND ITS SYSTEMATICS

We adopt a model for W production and detector response. We attempt to include in the model sufficient degrees of freedom to reflect the uncertainties in W production and detector response. These degrees of freedom are the parton distribution functions, the W p_T distribution for the sample, the lepton measurement resolution, the underlying event uncorrelated fluctuations, the p_T-dependent calorimeter response and resolution for recoil energy to the W p_T, and the net balance of transverse-energy flow parallel to the lepton direction, which includes lepton subtraction effects. For each of these effects, we determine what constraints may be applied to them from the data and the consequent limits on their contributions to systematic uncertainties in the W mass.

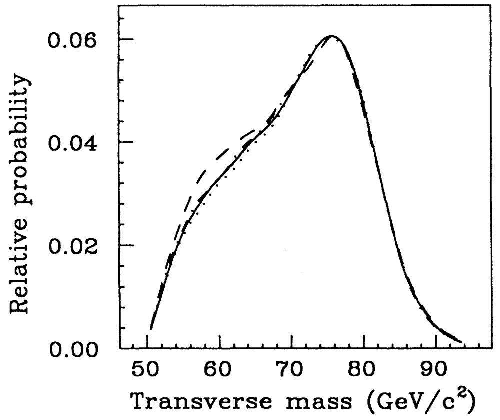

FIG. 24. Predicted m_T distribution for several choices of parton distribution functions. The solid line is MRS-B (Ref. 38), the dashed DFLM-2 (Ref. 37), the dotted DO-1 (Ref. 36), and the dot-dashed EHLQ-1 (Ref. 35).

The choice of fit range will be motivated by these systematic considerations and by the background considerations discussed in Sec. IX.

The Monte Carlo program generates W decays to leptons from the lowest-order QCD production process:

$$q\bar{q} \rightarrow W \; . \tag{11}$$

The program includes the W polarization in the decay:

$$W \rightarrow l\nu \; . \tag{12}$$

The simulation begins by generating the W rapidity, mass, and polarization distributions for the mass m_W, width Γ_W, and parton density being simulated. The parton density distributions are discussed in Sec. VIII A. The rapidity distribution reflects the parton distribution functions used to model the initial $p\bar{p}$ collision. The mass distribution reflects the convolution of the parton luminosities with an approximate[34] relativistic Breit-Wigner line shape:

$$\frac{dN}{dm_W} \sim \frac{s}{(s-m_W^2)^2+s^2\Gamma_W^2/m_W^2} \; . \tag{13}$$

We model only that part of the Breit-Wigner line shape that is within seven widths (Γ_W) of each nominal mass. We include the polarization distribution to model W^+'s coming from u quarks in the antiproton (or W^-'s from $\bar{u}$ quarks in the proton) which have the opposite helicity of the more plentiful W^+'s coming from u quarks in the proton. Rapidity y_i, mass m_i, and polarization P_i are chosen for the W from these distributions by rejection. The decay angle (θ_i^*) of the lepton (e or μ), in the rest frame of the W, is generated according to a $(1+P_i\cos\theta_i^*)^2$ distribution. Finally, a random lepton decay azimuth ϕ_i is generated. The lepton and neutrino four-vectors in the laboratory are calculated from m_i, y_i, θ_i^*, and ϕ_i.

The event vertex, the geometry of the detectors, the detector resolution, and the finite p_T of the W are simulated next. A z vertex is chosen from a Gaussian distribution of rms 30 cm truncated at ±60 cm (see Fig. 2). We propagate the boosted charged lepton from the vertex to the detector where the fiducial cuts are simulated. The rapidity cuts play a role in determining the detailed shape of the Jacobian peak.

We smear the lepton momentum with the appropriate resolution function. To obtain the reconstructed neutrino, the resolution of the calorimeter and its momentum-dependant response to the recoil of the W transverse momentum are modeled and an uncorrelated background event is added. The resolution parameters as well as the p_T of the W are discussed in Sec. VIII C. We offset $\not{u}_{\parallel}$ in the Monte Carlo program to match the data, as is discussed in Sec. VIII B. We finally require $p_T^l \geq 25$ GeV/c and $p_T^\nu \geq 25$ GeV/c as is done with the data sample.

We study the change in fit mass from variations of the model by fitting Monte Carlo samples generated appropriately.

A. Parton distribution functions

Several reasonable choices of parton distribution functions are used to simulate W production. We test Eichten-Hinchliffe-Lane-Quigg set 1[35] (EHLQ-1), Duke-Owens sets 1 and 2[36] (DO-1, DO-2), Diemoz-Ferroni-Longi-Martinelli sets 1–3[34] (DFLM-1, DFLM-2, DFLM-3), Martin-Roberts-Stirling set B (MRS-B), and MRS-E (Ref. 38) as a sample of the different possible assumptions we could make. We make MRS-B our standard choice. The differences between it and the other newer parton distribution functions (MRS-E and DFLM1–3) are small; these functions have been tuned more recently, expressly for the purpose of studying weak-boson production at the colliders.[38]

Varying the assumed structure of the proton varies the

TABLE I. Comparison of mass fit values for various choices of lower cutoff of the fit range. The upper cutoff is 94 GeV/c^2. All masses listed are in units of GeV/c^2. Monte Carlo samples are fit using a grid generated with the MRS-B parton distribution.

Lower cutoff	MRS-B	EHLQ-1	DO-1	DFLM-2
55 GeV	80.01±0.03	79.92±0.03	80.07±0.03	79.94±0.03
60 GeV	80.02±0.03	79.94±0.03	80.06±0.03	79.96±0.03
65 GeV (nominal)	80.01±0.03	79.94±0.04	80.00±0.03	79.94±0.04
70 GeV	80.03±0.04	79.93±0.04	79.95±0.04	79.94±0.04

TABLE II. Comparison of mass fit to Monte Carlo samples using different parton distribution functions (PDF's) for the nominal fit range 65–94 GeV/c^2. All masses listed are in units of GeV/c^2. The fitting grid used the MRS-B parton distribution.

PDF choice	Monte Carlo
MRS-B (nominal)	80.01±0.03
MRS-E	80.00±0.03
DFLM-1	79.96±0.03
DFLM-2	79.94±0.04
DFLM-3	79.97±0.03
DO-1	80.00±0.03
DO-2	79.99±0.03
EHLQ1	79.94±0.04

W longitudinal-momentum distribution. Figure 24 shows how the transverse-mass prediction varies with choice of parton distribution functions.

One Monte Carlo sample (with $m_W = 80.0$ GeV/c^2) is generated for each of the parton distributions tested. The overall model is otherwise fixed. We then fit these samples with our standard line shapes which use the MRS-B parton distribution set to give the values in Tables I and II.

Table I shows that for most parton distribution functions the mass is insensitive to the choice of lower cutoff. We choose 65 GeV/c^2 to limit our sensitivity to the choice of parton distribution function and to reduce further the potential background in our fits (see Sec. IX B). The largest deviation from the input mass is 60 MeV/c^2. We take 60 MeV/c^2 as an estimate of the uncertainty due to parton distribution functions.

B. Parallel balance

The distributions of the projections of the background event energy parallel and perpendiular to the charged lepton, $\not{u}_{\parallel}$ and $\not{u}_{\perp}$, are shown in Fig. 25. The offset after subtraction of the lepton energy (as described above) is -76 ± 115 MeV for the electron sample and -115 ± 150 MeV for the muon sample. These offsets are consistent with the expectations from the dijet requirement, which preferentially removes events with energy opposite the charged lepton. We match the average $\not{u}_{\parallel}$ in the model to the data. This procedure also accounts for possible imperfections in the lepton removal. Figure 26 shows

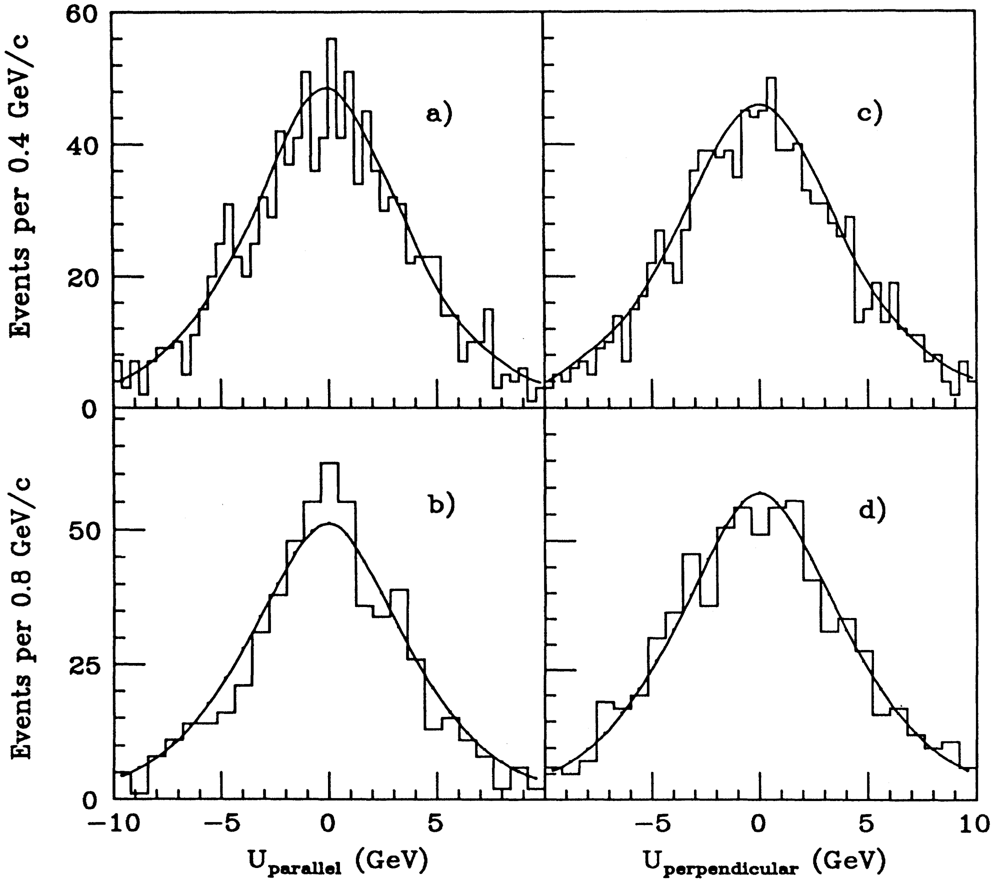

FIG. 25. Projection of the underlying event $\not{E}_T$ onto the charged-lepton direction ($\not{u}_{\parallel}$) (a) for electron events and (b) for muon events. The curves are the prediction of the model. The projection of the underlying event $\not{E}_T$ perpendicular to the charged-lepton direction ($\not{u}_{\perp}$) (c) for electron events and (d) for muon events.

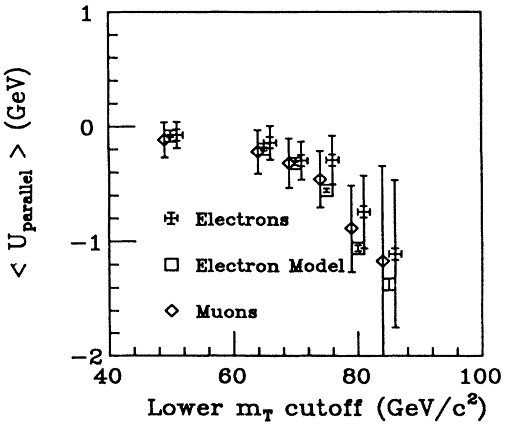

FIG. 26. Average $\not\!E_T$ along the charged-lepton direction ($\langle \not{u}_{\parallel} \rangle$) as a function of the m_T range of events used in the computation. The x axis gives the minimum m_T used; the maximum is 94 GeV/c^2. The muon model is tuned to reproduce the muon data over the range 50–94 GeV/c^2, giving slightly lower (40-MeV) average $\not{u}_{\parallel}$.

that the offset depends on the range of m_T included in its determination. The trend of the offset with m_T is well reproduced by the model. To allow for possible systematic error, we assume that only events with $m_T > 70$ GeV/c^2 influence the result; using only these events, the statistical matching accuracies become 150 and 215 MeV for the electron and muon samples. We note that to prevent possible pathological events from biasing the result, the offsets are computed using a ±10-GeV window about $\not{u}_{\parallel} = 0$ and that the statistical uncertainties correspond to the truncated distributions (see Fig. 25). The statistical accuracy of the $\not{u}_{\parallel}$ match corresponds to uncertainties in mass of 170 and 240 MeV/c^2 for the electron and muon samples, respectively.

C. Resolution and p_T^W

Several parameters in the model used in the Monte Carlo simulation contribute to the overall resolution. These are the lepton resolution, the underlying event resolution, the response and resolution in measuring the recoil to the W p_T, and the assumed input p_T^W distribution. We use other data to constrain all the parameters except the input p_T^W distribution, adjusting the latter to obtain internal consistency with the observed W data. We determine each uncertainty by varying the parameter within its constraints with all other parameters fixed. Although there are correlations (redundancy) among the parameters, we conservatively take the uncertainties to be independent. This part of the model has been tuned on the higher statistics W electron sample, and the resulting uncertainty (except for the charged-lepton resolutions) is common to both electron and muon samples.

Electron energy resolution was determined in test-beam studies to vary as $13.5\%/\sqrt{E_T}$ (E_T in GeV). There is an additional contribution of $(2.0\pm0.5)\%$ arising from cell-to-cell setting (1.7%) as well as systematic variations in mapping the response versus position and possible time variation. For a typical electron p_T of 35 GeV/c, the constant term contribution is substantial. Varying the constant term by ±0.5% gives rise to a 70-MeV variation in fit mass. This variation is quite conservative, changing the typical electron energy resolution of 2.9% from 2.6% to 3.3%.

For muons, the resolution is described by $\delta p_T/p_T = 0.0011 p_T$ (p_T in GeV/c), Gaussian in $1/p_T$. From the width of the E/p distribution (see Fig. 16) and the allowed variation in electron resolution, the tracking resolution is known to ±10%. If we vary this resolution by 10%, we obtain an 80-MeV/c^2 shift in fit mass for the muon sample.

We now turn to the uncorrelated underlying event; the recoil energy will be treated next. We assume that the characteristic azimuthally symmetric $\not\!E_T$ of this contribution should be similar to that of minimum-bias events, shown in Fig. 18. In the Monte Carlo simulation, the total E_T of an event is selected according to the observed distribution (Fig. 27), which has been corrected event by event for the E_T associated with the W recoil momentum. We take this associated E_T to be 1.4 times the nominally reconstructed p_T^W in order to reflect the angular spread in the energy flow, which is enhanced by the magnetic field. Varying this multiplier from 1.2 to 1.8 changes the fit mass by 20 MeV/c^2. Models with a correlation put in between the background event total E_T and p_T^W give no systematic shift in the mass. The added contribution (in GeV) per transverse component, taken from minimum-bias events, is given an rms of $(0.47\pm0.03)\sqrt{E_T}$ (E_T in GeV). The uncertainty corresponds to a mass variation of 90 MeV/c^2.

High-p_T W's are balanced by recoil energy in the form of jets. The actual recoil energy observed is lower because of the response in the calorimeter. For jets with a raw cluster energy of 20 GeV, the energy scale is depressed by a factor of 1.4.[18] Response to the 3–5-GeV

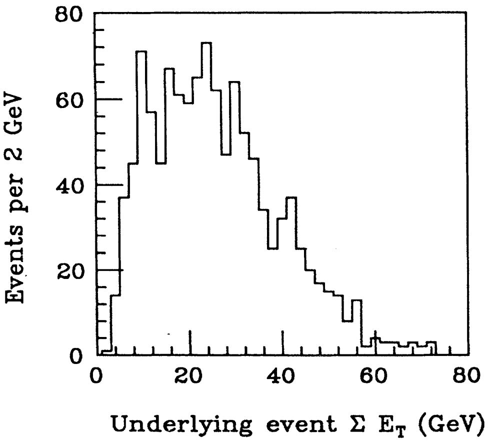

FIG. 27. Transverse energy observed accompanying the electron in W decay candidate events, corrected for the E_T associated with the W transverse momentum. This distribution is used as an input to the detector model of the neutrino resolution.

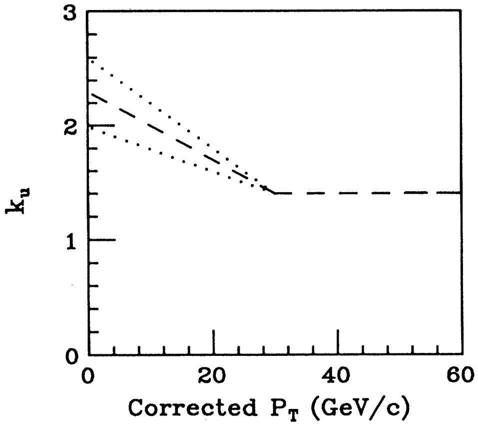

FIG. 28. Degradation factor k_u used in our model to simulate the effect of calorimeter nonlinearities and magnetic sweeping on the energy flow underlying W's. Above 30 GeV/c we use a constant factor of 1.4 to account for calorimeter nonlinearities. The extrapolation to lower p_T is constrained by the measurement of the hadronic recoil in dilepton decays of Z's (see also Fig. 29). The dotted lines indicate the constraint from the Z data.

recoil energy more typical of these W samples should be further depressed by magnetic sweeping and trapping. Charged particles with transverse momentum below 400 MeV/c will curl up in the magnetic field and not reach the central calorimeter.

The energy response of the calorimeter to the recoil energy is modeled by taking the observed nominal energy imbalance E_T^W to be given by p_T^W/k_u, where k_u is a piecewise continuous linear function of p_T^W as shown in Fig. 28. The parameters describing the response function at low values of p_T^W can be obtained from the study of transverse-momentum balance in Z events. We study the p_T balance along the lepton bisector azimuthal projection p_η (see Fig. 29). We assume that k_u is linear between 0 and 30 GeV/c in actual p_T^W and obtain a value of $k_u=2.3\pm0.3$ at $p_T^W=0$. For p_T^W of 30 GeV/c and above, we use the constant value $k_u^0=1.4$. The average value for k_u is 2.0 for our data sample. The uncertainty in determining the parameters of k_u vs p_T^W corresponds to an uncertainty of 50 MeV/c^2 in the W mass.

This recoil-energy imbalance (E_T^W) is smeared according to a Gaussian of width σ_{recoil}. A constraint on σ_{recoil} is obtained by unfolding the background event contribution from the p_η measurement in Z events. The result is $\sigma_{\text{recoil}}=(0.85^{+0.30}_{-0.20})\sqrt{p_T}$. The uncertainty in σ_{recoil} corresponds to an uncertainty of 60 MeV/c^2 in the W mass. The direction is not smeared.

For a given set of model parameters, we empirically unfold an input p_T^W distribution, forcing the output distribution to agree with the observed p_T^W distribution. The input distribution and the output and observed distributions are shown in Fig. 30. The average of the input p_T distribution is constrained to ±4%, corresponding to a 20-MeV/c^2 shift in fit mass. Note that this is not a measurement of any actual p_T^W spectrum, even for this highly

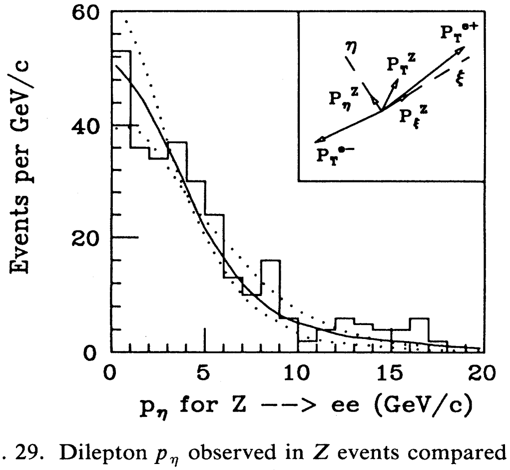

FIG. 29. Dilepton p_η observed in Z events compared to our model's prediction (solid line). The inset shows the η-ξ coordinate system. Since the leptons tend to be back to back, p_η is largely determined by track angles. To the extent that the W and Z p_T distributions should be the same at low p_T this shows that our model includes an appropriate W p_T. The dotted lines show the relatively normalized predictions for 1σ variations of k_u.

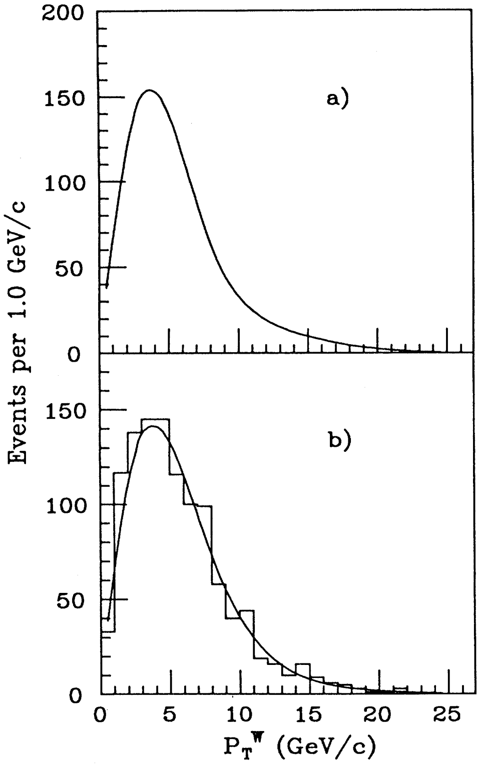

FIG. 30. (a) Input p_T distribution of the W candidates unfolded from the observed distribution using the model. (b) Agreement between the observed W p_T distribution and the simulation.

biased sample, but only a constraint within the model. For example, varying the recoil response at $p_T^W=0$ within its nominal error results in an ±11% variation in average p_T^W. Variations in the skew (the first moment, holding the mean constant) of the assumed input p_T^W distribution can give 50-MeV/c^2 shifts in fit mass.

The overall systematic uncertainty due to uncertainty in resolutions and p_T^W distribution, adding all contributions in quadrature, is then 145 MeV/c^2 for electrons and 150 MeV/c^2 for muons. These include 130 MeV/c^2, which is common to the two samples, coming from underlying event energy and resolution, recoil response and resolution, and the allowed variation of the input p_T^W distribution.

D. Summary of uncertainties of the model

The contributions to the uncertainty of the W mass due to systematic uncertainties in the model are (1) 60 MeV/c^2 for parton distribution functions, (2) 130 MeV/c^2 for underlying event resolution and p_T^W (common to e and μ), (3) 70 and 80 MeV/c^2 for electron and muon resolutions, and (4) 170 and 240 MeV/c^2 for calorimeter energy balance parallel to the electrons and muons.

IX. RESULTS AND SYSTEMATICS

The results of the fits with Γ_W constrained to 2.1 GeV are 79.84±0.35(stat) GeV/c^2 for the electron sample and 79.78±0.53(stat) GeV/c^2 for the muon sample (see Fig. 21).

These results need to be corrected to account for internal QED radiation. Collinear radiation for electrons is accounted for in the calibration procedure (Sec. IV B), and external radiation is small for muons. A radiative simulation[39] is used to predict the angles and energies of radiated photons. These photons reduce the observed W mass. We treat the photon appropriately according to its distance from the lepton in the calorimeter cells. The results are not sensitive to assumptions about the efficiency of observing low-energy photons. The predicted mass shifts are 70±10 MeV/c^2 for electrons and 125±10 MeV/c^2 for muons.

A. Uncertainty in the fitting procedure

As discussed in Sec. VII, we have assigned 50 MeV/c^2 of uncertainty to the fitting procedure. We check the overall statistical uncertainties by comparing the spread in fit values and uncertainties of a large number of Monte Carlo samples of the same size as the electron and muon samples. These are shown in Fig. 31. The statistical uncertainties for our fits to the data are typical.

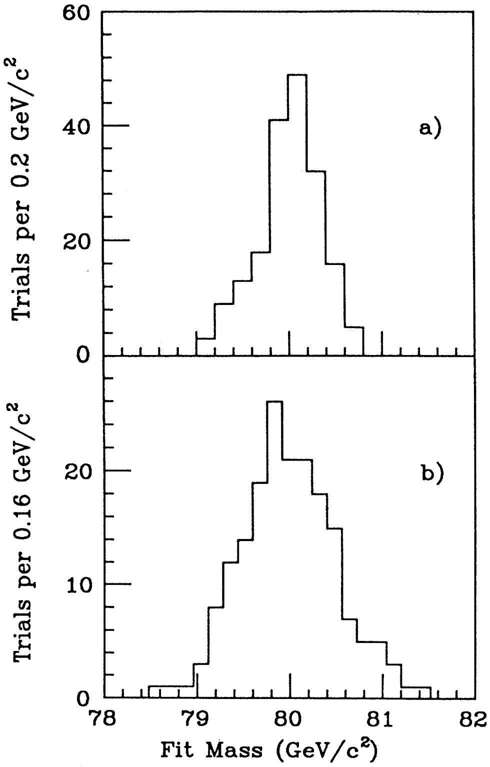

FIG. 31. Spread in fit masses obtained from 200 simulated event samples containing (a) 1130 and (b) 600 events (the number of events in our respective fit samples). We use the spread in this distribution to check the statistical uncertainty obtained from the fits.

B. Backgrounds

We consider several sources of background in the W sample. The sequential decay $W \rightarrow \tau \rightarrow$ leptons mimics the direct decay; however, the resulting m_T distribution is softer [see Fig. 32(a)]. We simulate a large sample of these sequential decays [using the ISAJET (V6.12) (Ref. 40) $p\bar{p}$ physics simulation] and conclude that only 4 events should enter the electron sample, with only 1.5 events entering the fit ($m_T \geq 65$ GeV/c^2). We add 10 times the predicted τ background to our data sample and scale down the result; we predict a 4-MeV shift in W mass.

For the electron sample, another estimate of potential background comes from the photon conversion analysis discussed above. The measured inefficiency of the conversion filter is about 20%. Even if the 3% of events removed by the conversion filter are all assumed to be background, less than 1% background can remain. If we add the conversion events [see Fig. 32(b)] to the electron sample and refit, the mass is lowered by 40 MeV/c^2.

Z events, where one of the charged leptons is lost, mimic W events. This could be an important background as Z charged leptons can have higher momenta. However, the cross section for $Z \rightarrow ll$ production is 10 times lower than that for $W \rightarrow l\nu$ production.[41] The jet veto (see Sec. VI) eliminates events with second electrons producing E_T greater than 7 GeV in the calorimeter. In addition, we remove events with second tracks above 15 GeV/c in both electron and muon samples. We simulate the production and decay of Z's and find only 0.1% satisfy our W electron selection criteria. This predicts only one such event in our electron W sample. The Z's that survive tend to have an m_T distribution similar to that of the τ's. We conclude this has a negligible effect on our fit

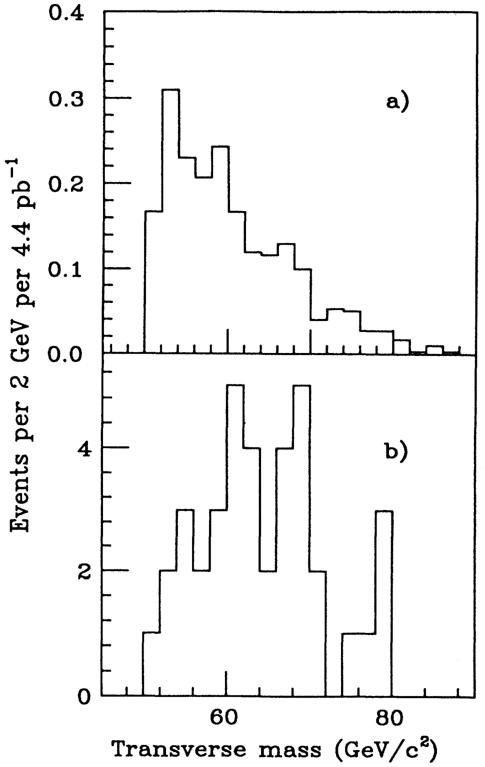

FIG. 32. (a) ISAJET (V6.12) prediction of the m_T distribution for charged leptons from the sequential decay $W \rightarrow \tau \rightarrow e$. These exhibit a softer m_T distribution and could shift the mass downwards since they are not included in the model. (b) m_T distribution of conversion candidates selected by our filter. These are consistent with the over efficiency of our filter.

mass. In the muon sample, we estimate that an upper limit on the number of remaining Z's is 4%. Adding a 4% background consistent with the shape of the Z's changes the mass by 20 MeV/c^2.

Finally, we have studied the effect a flat background would have on the fit mass. Adding even a 1% background of this form shifts the electron sample mass up by only 70 MeV/c^2. We take 50 MeV/c^2 as the potential uncertainty in the W mass due the presence of background in the electron sample.

Cosmic rays are a significant background to the muon sample. We estimate that the number of cosmic rays that remain in the muon sample is less than 0.4%. This spectrum is approximately flat. A 1% flat background to the muon sample increases the fitted W mass by 110 MeV/c^2. We take 110 MeV/c^2 as the uncertainty in the W mass due to background in the muon sample.

C. Summary of uncertainties

The nontrivial uncertainties for the W mass determination are summarized in Table III. For the electron and muon samples, the statistical uncertainties are 350 and 530 MeV/c^2, respectively. The energy scale uncertainties are 190 and 80 MeV/c^2, and all other systematics are 240 and 315 MeV/c^2. The uncertainties common to both electron and muon data samples are 80 MeV/c^2 for the chamber tracking scale, 60 MeV/c^2 for parton distribution functions, 130 MeV/c^2 for the underlying event model, and 50 MeV/c^2 for systematic due to fitting. The energy scale uncertainties are common with the respective CDF Z mass samples.

TABLE III. Uncertainties in the W mass measurement. All uncertainties are quoted in units of MeV/c^2. In parentheses are the statistical (and overall) mass uncertainties if Γ_W is determined in the fit as well. The scale uncertainties are in common with the Z mass measurement (Ref. 6). The uncertainties which are the same for both samples are listed as common.

Uncertainty	Electrons	Muons	Common
Statistical	350 (440)	530 (650)	
Energy scale	190	80	80
(1) Tracking chamber	80	80	80
(2) Calorimeter	175		
Systematics	240	315	150
(1) Proton structure	60	60	60
(2) Resolution, W p_T	145	150	130
(3) Parallel balance	170	240	
(4) Background	50	110	
(5) Fitting	50	50	50
Overall	465 (540)	620 (725)	

D. Systematic checks

As a check for pathologies, we have subdivided the data by lepton charge, time during the data taking, and geography in the detector (proton or antiproton direction). None of these subsets show significant variation. The lepton sign selected samples give fit masses (in GeV/c^2) for positive leptons of 80.06±0.49 and 79.11±0.74 and for negative leptons of 79.77±0.50 and 80.41±0.76 for electrons and muons, respectively (statistical uncertainty only). These values correspond to a mass difference $m(W^+ - W^-) = -0.19 \pm 0.58$ GeV/c^2, consistent with expectations from CPT conservation. As check for bias in the $\not{E}_T$ selection of electron events, we use a sample selected with the electron cuts discussed in Sec. IV. This sample of 1128 events, of which 1018 are common to both electron samples, gives $m_W = 80.02 \pm 0.35$(stat). The nominal sample gives $m_W = 79.84 \pm 0.35$(stat). We have checked for pathology in the details of selecting clean event topologies by repeating the electron analysis, dropping the jet cut at 7 GeV, and requiring $p_T^W < 20$ GeV/c. This results in a 1420-event sample. We repeat the exercise for this new sample of determining an appropriate input p_T^W distribution as well as the electron subtraction parallel balance. The mean p_T^W in this case is 6.8 GeV/c (to be compared with 5.6 GeV/c in our standard sample), and the shape of the input distribution is different. The resulting fit mass is lower than the nominal fit by 100 MeV/c^2.[42] We find

TABLE IV. Comparison of mass and width fit values for various choices of upper cutoff of fit range for the electron sample. All masses listed in GeV/c^2 and widths in GeV/c. These particular Monte Carlo samples had $m_W = 80$ GeV/c^2 and $\Gamma_W = 2.2$ GeV.

	Width floated		
Cutoff (GeV/c^2)	Fit to data (m_W;Γ_W)	χ^2/N_{DF}	Fit to Monte Carlo samples
98	79.61±0.41;2.6±0.5	24.5/30	79.98±0.05;2.29±0.07
96	79.59±0.42;2.7±0.6	23.7/28	79.96±0.05;2.31±0.08
94 (nominal)	79.53±0.43;3.0±0.5	22.1/26	79.98±0.05;2.39±0.10
92	79.41±0.43;3.7±0.7	19.8/26	79.95±0.05;2.43±0.11
90	79.43±0.37;3.7±0.8	17.9/22	79.92±0.09;2.59±0.34
	Width constrained		
Cutoff (GeV/c^2)	Fit to data (m_W)	χ^2/N_{DF}	Fit to Monte Carlo samples
98	79.87±0.34	27.3/31	80.01±0.03
96	79.82±0.34	26.0/29	80.03±0.03
94 (nominal)	79.84±0.35	25.4/27	80.01±0.03
92	79.86±0.35	25.1/25	80.04±0.04
90	79.78±0.36	21.0/23	80.01±0.04

no evidence for systematic effects. The systematic uncertainties for this fit are larger than in our usual analysis.

In our analysis we scaled the underlying event energy by a factor of $k_u^0 = 1.4$. While this may be best for those events with large p_T^W, we investigate the effect of changing k_u^0 from 1.0 to 1.8. Setting $k_u^0 = 1.0$ and repeating the electron fit, we find $m_W = 79.92 \pm 0.34$(stat) GeV/c^2, while setting $k_u^0 = 1.8$, we find $m_W = 79.79 \pm 0.37$(stat) GeV/c^2. These changes in fit mass show no evidence for additional systematic uncertainty. Studies of large simulated samples with different values of k_u^0 show no change in the fit mass.

If we change the upper limit to the fit range, we observe variations in the fit mass and width as shown in Table IV for electrons and Table V for muons. The fixed-width fits are more stable than the variable-width fits when we change the model resolutions. The likelihood contours showing the mass-width correlation are shown in Fig. 23.

As a further check, we also fit the lepton p_T spectra. These are shown in Fig. 33. Of the parameters in the underlying event model, the shapes of the charged-lepton spectra are sensitive only to the assumed p_T^W distribution and lepton resolution. The tests described in Sec. VIII vary one parameter of the model at a time. To evaluate the systematic uncertainty for fits to lepton spectra, we vary parameters in the model and extract a new input p_T^W distribution. We then vary the p_T^W within its constraints and find changes of up to 250 MeV/c^2 in the fit mass. The calibration, proton structure, background, and fitting uncertainties affect the charged-lepton spectra in the same way as the m_T spectra. The parallel energy balance does not affect the fits to the charged-lepton p_T spectra. We obtain 430- and 310-MeV/c^2 overall systematic un-

TABLE V. Comparison of mass and width fit values for various choices of upper cutoff of fit range for the muon sample. All masses listed in GeV/c^2 and widths in GeV/c. These particular Monte Carlo samples had $m_W = 80$ GeV/c^2 and $\Gamma_W = 2.2$ GeV.

	Width floated		
Cutoff (GeV/c^2)	Fit to data (m_W;Γ_W)	χ^2/N_{DF}	Fit to Monte Carlo samples
98	79.46±0.64;3.4±1.0	34.2/30	80.01±0.04;2.19±0.05
96	79.69±0.65;2.3±1.0	29.7/28	80.01±0.05;2.18±0.06
94 (nominal)	79.68±0.65;2.3±1.1	29.3/26	80.00±0.04;2.18±0.07
92	79.90±0.25;0.4±1.5	25.9/24	80.01±0.04;2.17±0.07
90	79.97±0.61;0.4±2.3	25.9/22	80.00±0.04;2.28±0.07
	Width constrained		
Cutoff (GeV/c^2)	Fit to data (m_W)	χ^2/N_{DF}	Fit to Monte Carlo samples
98	80.06±0.52	33.8/31	80.00±0.04
96	79.76±0.52	29.6/29	80.00±0.04
94 (nominal)	79.78±0.53	29.1/27	80.00±0.04
92	79.54±0.54	26.5/25	80.00±0.04
90	79.69±0.57	26.1/23	80.02±0.04

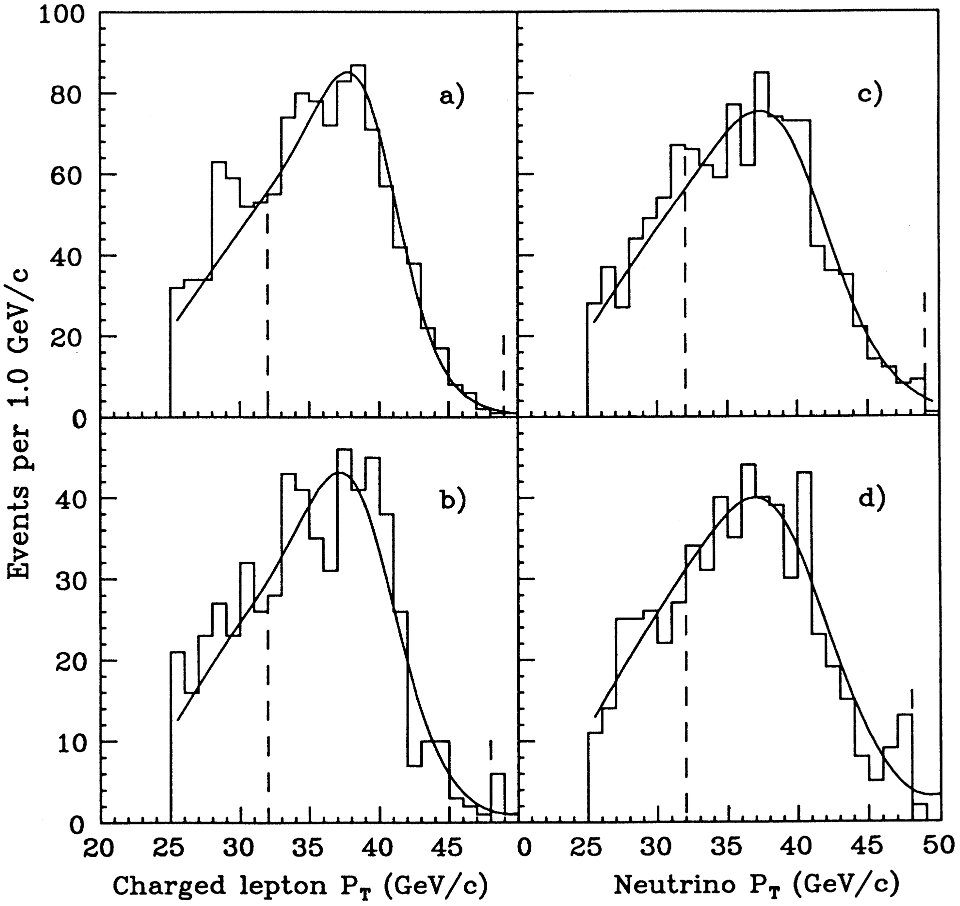

FIG. 33. Charged-lepton p_T distribution for all (a) electron and (b) muon W candidates, selected for measuring the mass. The corresponding neutrino p_T distribution (c) for the electron sample and (d) for the muon sample. The best fit to the data is overlaid in each case.

certainties to m_W derived from the electron and muon p_T fits, respectively. The electron spectrum fit gives $m_W = 80.06 \pm 0.40(\text{stat}) \pm 0.43(\text{syst})$ GeV/c^2. The muon spectrum fit gives $m_W = 79.44 \pm 0.56(\text{stat}) \pm 0.31(\text{syst})$ GeV/c^2.

Fitting the neutrino p_T spectra, we find $m_W = 80.20 \pm 0.52(\text{stat}) \pm 0.55(\text{syst})$ GeV/c^2 and $m_W = 79.89 \pm 0.78(\text{stat}) \pm 0.48(\text{syst})$ GeV/c^2 for the electron and muon samples. We estimate an uncertainty of 330 MeV/c^2 due to the assumed input p_T^W distribution determined as was described previously for the fit to the charged-lepton spectra. The neutrino distributions are also quite sensitive to the modeling of the underlying event and detector resolution.

The consistency of these fits lend credibility to the m_T fits. We use the latter for our final results. None of the fit values quoted above include radiative corrections.

E. Final results

After adding the radiative correction, the final result from the W electron m_T distribution is

$$m_W^e = 79.91 \pm 0.35(\text{stat}) \pm 0.24(\text{syst}) \pm 0.19(\text{scale})\ \text{GeV}/c^2 \ . \tag{14}$$

The final result for the muon m_T distribution is

$$m_W^\mu = 79.90 \pm 0.53(\text{stat}) \pm 0.32(\text{syst}) \pm 0.08(\text{scale})\ \text{GeV}/c^2 \ . \tag{15}$$

The two CDF W mass measurements may be combined, keeping track of common uncertainties discussed above, to give

$$m_W^{\text{CDF}} = 79.91 \pm 0.39\ \text{GeV}/c^2 \ . \tag{16}$$

X. IMPLICATIONS OF THE MEASUREMENT

The CDF measurement may be compared to the recent UA2 absolute result[43] of

$$m_W^{\text{UA2}} = 80.79 \pm 0.31(\text{stat}) \pm 0.21(\text{syst}) \pm 0.81(\text{scale})\ \text{GeV}/c^2 \ . \tag{17}$$

In order to obtain improved accuracy, the UA2 quotes the value taking their energy scale by matching their measured Z mass to more accurate determinations from LEP.[43] We can duplicate this exercise and take our scale from the PDG Z mass value of 91.161 ± 0.031 GeV/c^2.[30] Although our scale uncertainty in this case becomes irrelevant as it is common to the W and Z mass measurements, the larger statistical uncertainty on our Z measurements must be included. The result is $m_W=79.92\pm0.45$ GeV/c^2 for the two samples combined. This compares to the UA2 measurement (scaled to a Z mass of 91.15 GeV/c^2) of $m_W=80.49\pm0.49$ GeV/c^2. The results of both experiments, each optimally obtained, combine to give

$$m_W^{\rm CDF+UA2}=80.13\pm0.31\ {\rm GeV}/c^2\ . \tag{18}$$

We measure the weak mixing angle using the definition

$$\sin^2\theta_W\equiv 1-\frac{m_W^2}{m_Z^2}\ . \tag{19}$$

Using CDF measurements alone, we obtain $\sin^2\theta_W=0.235\pm0.010$ and 0.224 ± 0.014 for the electron and muon samples, respectively. The uncertainty in the electron sample includes (in quadrature) ±0.0015 as a systematic effect of possible nonlinearity in the calorimeter electron measurement. The two results may be combined to give $\sin^2\theta_W=0.231\pm0.008$. A more accurate result uses our absolute W mass and the world average Z mass to give

$$\sin^2\theta_W=0.2317\pm0.0075\ . \tag{20}$$

This measurement has implications for the possible mass of the as-yet unfound top quark. These implications are summarized in Fig. 34. The measurement of the weak mixing angle is applied to calculations[44] of predictions as a function of assumed top mass. The results are consistent with the absence of a top signal in CDF searches.[23,24,45] The allowed region corresponds to a top mass below 220 GeV/c^2 (95% C.L.).

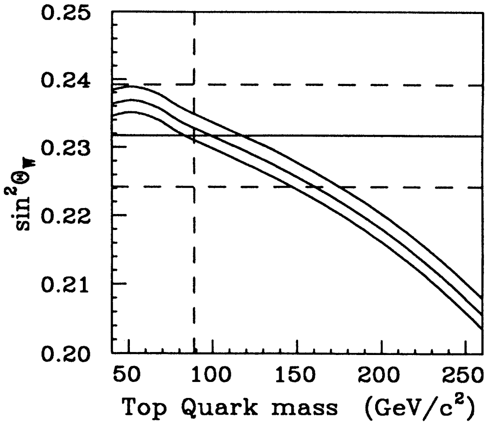

FIG. 34. Comparison of the weak-mixing-angle measurements from $\sin^2\theta_W$ using the world-average Z mass and our W mass measurement with radiative predictions (Ref. 44) using a Z mass of 91.161 GeV/c^2, as a function of assumed mass for the top quark. The 89-GeV/c^2 lower-limit top mass (95% C.L.) is from Ref. 45. The curves, from top to bottom, correspond to Higgs-boson masses of 1000, 250, and 50 GeV/c^2.

This measurement of $\sin^2\theta_W$ may be combined with the UA2 result of 0.2202 ± 0.0095 (Ref. 43) to give an overall result from direct mass measurements in hadron collisions of $\sin^2\theta_W=0.227\pm0.006$. The combined value corresponds to a top mass below 230 GeV/c^2.

ACKNOWLEDGMENTS

We thank the Fermilab Accelerator Division for their exceptional performance in the operation of the Tevatron and the Antiproton Source. This work was supported in part by the Department of Energy, the National Science Foundation, Istito Nazionale di Fisica Nucleare, the Ministry of Science, Culture, and Education of Japan, and the A. P. Sloan Foundation.

---

[*] Permanent address: Albert-Ludwig University, Freiburg, Germany.

[†] Permanent address: University of Oxford, Oxford, England.

[‡] Permanent address: Università di Bologna, Bologna, Italy.

[1] S. L. Glashow, Nucl. Phys. **22**, 579 (1961).

[2] S. Weinberg, Phys. Rev. Lett. **19**, 1264 (1967).

[3] A. Salam, in *Elementary Particle Theory: Relativistic Groups and Analyticity (Nobel Symposium No. 8)*, edited by N. Svartholm (Almqvist and Wiksell, Stockholm, 1968), p. 367.

[4] UA1 Collaboration, G. Arnison *et al.*, Europhys. Lett. **1**, 327 (1986).

[5] UA2 Collaboration, R. Ansari *et al.*, Phys. Lett. B **186**, 440 (1987).

[6] CDF Collaboration, F. Abe *et al.*, Phys. Rev. Lett. **63**, 720 (1989).

[7] Mark II Collaboration, G. Abrams *et al.*, Phys. Rev. Lett. **63**, 2173 (1989).

[8] L3 Collaboration, B. Adeva *et al.*, Phys. Lett. B **231**, 509 (1989).

[9] ALEPH Collaboration, D. Decamp *et al.*, Phys. Lett. B **231**, 519 (1989).

[10] OPAL Collaboration, M. Akrawy *et al.*, Phys. Lett. B **231**, 530 (1989).

[11] DELPHI Collaboration, P. Aarnio *et al.*, Phys. Lett. B **231**, 539 (1989).

[12] CDF Collaboration, F. Abe *et al.*, Nucl. Instum. Methods A **271**, 387 (1988).

[13] F. Snider *et al.*, Nucl. Instrum. Methods A **268**, 75 (1988).

[14] F. Bedeschi *et al.*, Nucl. Instrum. Methods A **268**, 50 (1988).

[15] G. Ascoli *et al.*, Nucl. Instrum. Methods A **267**, 218 (1988).

[16] L. Balka *et al.*, Nucl. Instrum. Methods A **267**, 272 (1988).

[17] S. R. Hahn *et al.*, Nucl. Instrum. Methods A **267**, 351 (1988).

[18] CDF Collaboration, F. Abe *et al.*, Phys. Rev. Lett. **62**, 613 (1988). This reference provides a description of how we cluster energy into jetlike objects.

[19] D. Amidei *et al.*, Nucl. Instrum. Methods A **267**, 51 (1988).

[20] G. Ascoli *et al.*, Nucl. Instrum. Methods A **267**, 272 (1988).

[21] G. W. Foster *et al.*, Nucl. Instrum. Methods A **269**, 93 (1988).

[22] The trigger clustering scheme searches for trigger towers with more than 3 GeV of energy and groups all adjacent towers with more than 2.5 GeV of energy into a cluster.

[23] CDF Collaboration, F. Abe *et al.*, Phys. Rev. Lett. **64**, 142 (1990).

[24] CDF Collaboration, F. Abe *et al.*, Phys. Rev. Lett. **64**, 147 (1990).

[25] D. A. Smith, Ph.D. thesis, University of Illinois at Urbana-Champaign, 1989.

[26] T. Carroll *et al.*, Nucl. Instrum. Methods A **263**, 199 (1988).

[27] A software electron cluster starts with any EM calorimeter cell above 3 GeV and absorbs all adjacent cells with more than 0.1 MeV. To remain an electron candidate, no more than 12.5% of the cluster energy can appear in the hadron calorimeter.

[28] D. Brown, Ph.D. thesis, Harvard University, 1989.

[29] CDF Collaboration, F. Abe *et al.*, Phys. Rev. Lett. **62**, 1005 (1989).

[30] Particle Data Group, J. J. Hernández *et al.*, Phys. Lett. B **239**, 1 (1990).

[31] K. Yasuoka *et al.*, Nucl. Instrum. Methods A **267**, 315 (1988).

[32] F. James and M. Roos, CERN Program Library documentation, 1983.

[33] W. Press, B. Flannery, S. Teukolsky, and W. Vetterling, *Numerical Recipes* (Cambridge University Press, Cambridge, England, 1986), Chap. 3, pp. 97–101.

[34] R. N. Cahn, Phys. Rev. D **36**, 2666 (1987).

[35] E. Eichten, I. Hinchliffe, K. Lane, and C. Quigg, Rev. Mod. Phys. **56**, 579 (1984).

[36] D. Duke and J. F. Owens, Phys. Rev. D **30**, 49 (1984).

[37] M. Diemoz, F. Ferroni, E. Longo, and G. Martinelli, Z. Phys. C **39**, 21 (1988).

[38] A. D. Martin, R. G. Roberts, and W. J. Stirling, Phys. Rev. D **37**, 1161 (1988).

[39] R. G. Wagner [unpublished, based on calculations by F. Behrends *et al.*, Z. Phys. C **27**, 155 (1985)]; F. Behrends and R. Kleiss, *ibid.* **27**, 365 (1985).

[40] F. Paige and S. D. Protopopescu, Brookhaven National Laboratory Technical Report No. BNL 38034 (unpublished).

[41] CDF Collaboration, F. Abe *et al.*, Phys. Rev. Lett. **64**, 152 (1990).

[42] William Trischuk, Ph.D. thesis, Harvard University, 1990.

[43] UA2 Collaboration, J. Alitti *et al.*, Phys. Lett. B **241**, 150 (1990).

[44] We wish to thank Duncan Morris for the use of his computer program in generating Fig. 34. See also W. Hollik *et al.*, Fortsch. Phys. **38**, 165 (1990).

[45] K. Sliwa, in *High Energy Hadronic Interactions,* proceedings of the XXVth Rencontres de Moriond, Les Arcs, France, 1990, edited by J. Tran Thanh Van (Editions Frontieres, Gif-sur-Yvette, 1990).

[46] Philip Schlabach, Ph.D. thesis, University of Illinois at Urbana-Champaign, 1990.